Simple and extensible plate and shell finite element models through automatic code generation tools

Jack S. Hale[a], Matteo Brunetti[b,c], Stéphane P. A. Bordas[a,d], Corrado Maurini[c,*]

[a] *Institute of Computational Engineering, University of Luxembourg, Luxembourg.*
[b] *Dipartimento di Ingegneria Strutturale e Geotecnica, Sapienza Università di Roma, Italy.*
[c] *Sorbonne Université, CNRS, Institut Jean Le Rond d'Alembert, UMR 7190, F-75005, Paris, France.*
[d] *School of Engineering, Cardiff University, United Kingdom.*

Abstract

A large number of advanced finite element shell formulations have been developed, but their adoption is hindered by complexities of transforming mathematical formulations into computer code. Furthermore, it is often not straightforward to adapt existing implementations to emerging frontier problems in thin structural mechanics including nonlinear material behaviour, complex microstructures, multi-physical couplings, or active materials. We show that by using a high-level mathematical modelling strategy and automatic code generation tools, a wide range of advanced plate and shell finite element models can be generated easily and efficiently, including: the linear and non-linear geometrically exact Naghdi shell models, the Marguerre-von Kármán shallow shell model, and the Reissner-Mindlin plate model. To solve shear and membrane-locking issues, we use: a novel re-interpretation of the Mixed Interpolation of Tensorial Component (MITC) procedure as a mixed-hybridisable finite element method, and a high polynomial order Partial Selective Reduced Integration (PSRI) method. The effectiveness of these approaches and the ease of writing solvers is illustrated through a large set of verification tests and demo codes, collected in an open-source library, FEniCS-Shells, that extends the FEniCS Project finite element problem solving environment.

Keywords: thin structures, plates, shells, finite element methods, domain specific language, FEniCS.

1. Introduction

Plates and shells are solids occupying a spatial domain with one dimension, the thickness, much smaller than the others. This implies the possibility of experiencing large changes of shape even with small material deformations and an approximately linear elastic material behaviour. Their study has received renewed attention in the last decade because of their unique nonlinear behaviour, mainly caused by geometric effects [12], leading to d-cone singularities and crumpling [33], fracture [84], or multistability [89, 90]. Examples of modern application fields in engineering include shape control through active materials [52, 43], stretchable electronics [81], soft robotics [63], and thin nano-structures e.g. graphene sheets and nanotubes [11].

*Corresponding author
Email address: corrado.maurini@upmc.fr (Corrado Maurini)

Effective models for plates and shells are two-dimensional, the through-the-thickness kinematics being described by including a suitable microstructure in the model. Their mathematical modelling leads to set of non-linear partial differential equations (PDEs) defined on a two-dimensional manifold embedded in three-dimensional space. The resulting PDEs can be discretised using a variety of numerical techniques, e.g. finite element methods (FEM) [15, 76], isogeometric analysis [49, 20], and meshfree methods [42]. FEM-based discretisations of the plate and shell models are available in both commercial (see e.g. Abaqus [2], AceFem [56] and Adina [14] and Ls-Dyna) and open-source (e.g. GetFem++ [77], IgaFem [75], Code_Aster [34], Mat-Fem [1] and Elmer [78]) software packages. However, formulating the mathematical models and implementing finite element solvers for custom plates and shells models remains a complex, highly technical, and time-consuming task, requiring advanced knowledge in differential geometry, numerical analysis, and mechanics. Shell and plate finite element models are regarded as very advanced topics in structural engineering and applied mathematics curricula, and rarely are graduate students trained in their implementation.

Our work aims to overcome some of the above difficulties by using modern automatic code generation tools and suitable mathematical abstractions. We present easily extensible and customisable methods for the implementation of finite element solvers for various models of thin structures, ranging from linear plates to non-linear shells. We leverage the tools offered by the finite element library FEniCS Project [4], in particular its Unified Form Language (UFL) [5] and the associated FEniCS Form Compiler (FFC) [50], to allow users to straightforwardly formulate complex custom nonlinear shell models with less than one hundred lines of Python code and syntax that closely mirrors the mathematical abstractions of the variational formulation. We exploit the symbolic processing capabilities of UFL to specify the potential energy functionals of various thin structural models in a high-level way and select suitable locking-free finite element spaces for their discretisation. Custom constitutive models are straightforward to implement. Consistent linearisation of the potential energy functional is performed automatically using the symbolic differentiation tools in UFL [5]. These symbolic expressions are compiled automatically to finite element code using FFC [50]. The differential geometry concepts [31] are expressed directly in a very simple and expressive format, which we believe is of great pedagogical value. We mimic the geometrically-exact shell model [31], where the reference configuration is described by a mapping from $\mathbb{R}^2$ to a surface embedded in Euclidean space. Although we do not discuss here the implementation of specific preconditioners, our finite element solvers can run without modification on high-performance computing architectures using MPI and PETSc [13] allowing large-scale calculations to be performed. State-of-the-art linear and non-linear solution strategies are immediately available through PETSc [13]. These aspects sum up to a unique approach that we believe will be of value to researchers, students, and practitioners working on frontier problems in the mechanics of thin structures. The outcome of our work is distributed in the form of an open-source (LGPLv3) Python library, FEniCS-Shells [39], collecting an implementation of the models and discretisation techniques presented in this paper and including a large set of examples and documented demos.

We consider here several *shearable* plate and shell models, including linear plates (Reissner-Mindlin model [80, 70]), linear and nonlinear shells (Nagdhi model [72, 71]), and weakly non-linear shallow shells (Marguerre-von Kármán model [67]). For these structural models, the discretisation strategy is particularly important, because shear and membrane locking can lead to an unacceptably slow convergence rate of the finite element solution with the mesh size [28]. After a deep analysis of the methods available in the literature and the possible software tools, we selected two main

discretisation techniques: the popular Mixed Interpolation of Tensorial Components (MITC) approach [15, 16, 35] and a high polynomial-order Partial Selective Reduced Integration (PSRI) approach [9], both of which can be applied in a uniform manner across user-defined models.

Both the MITC and PSRI approches presented here include some original aspects with respect to the formulations previously introduced in the literature. In order to fit within the abstractions of UFL and the associated code generation tools, MITC is reformulated as a mixed hybridisable variational form with element-wise local projection. The PSRI technique proposed in [9] is extended to nonlinear shells with a modified reduced integration rule and optimised weighting factor for the energy splitting. To provide an efficient parallel implementation of the MITC technique, we also extended the FEniCS automatic assembly tools to include the possibility of eliminating local degrees of freedom through static condensation, a feature that could be potentially ported to the FEniCS library itself in the near future.

To verify the convergence of the adopted MITC and PSRI discretisation techniques and illustrate the capability of the FEniCS-Shells library, we report a a large set of numerical benchmark and verification tests. Beside many classical examples, we propose a novel numerical benchmark problem based on the exact solution of Mansfield [64] for the thermal buckling of a lenticular plate. We believe that this latter example can usefully complement the traditional gallery of verification tests for plates and shells.

The paper is organised as follows. First, we give an overview of the structural models considered in our work, presenting the research of their equilibrium configurations as an energy minimisation problem (Section 2). Hence we discuss the mathematics behind their finite element discretisation and some details about their practical implementation (Section 3). Finally we show some comprehensive verification examples demonstrating what is possible with our approach and the performance of the proposed methods (Section 4). Three detailed documented demos are included as supplementary material and several more are available in the online repository of the python library FEniCS-Shells, companion to this paper.

A permanent DOI [39] has been created with links to the latest code and documentation. Table 1 summarises the mathematical models and the numerical methods presented in each of the documented demos currently available online. The two adopted discretisation techniques, MITC and PSRI, can in principle be applied indifferently to the different models. We mainly suggest to use MITC for curing shear-locking in linear plates and PSRI in non-linear shells, because the specific MITC formulation that we implemented turns out to be less effective for membrane locking (see *e.g.* the examples of Section 4.3). However all the combinations of models and discretisations are in principle possible and the users can easily adapt the provided demos to new models and implement variants of the available discretisations. We suggest the reader consult the demos to have an overview of the main capabilities and features of FEniCS-Shells, and in particular the *Clamped Reissner-Mindlin plate under uniform load* demo for linear plates, the *Buckling of a heated von-Kármán plate* for weakly nonlinear plate models, and the *Clamped semi-cylindrical Naghdi shell under point load* demo for fully nonlinear shells. FEniCS-Shells follows the *Best Practices for Scientific Computing* [96] as closely as possible, including using version control, continuous integration and testing, repeatable computing environments [40] and providing thorough documentation.

Title	Model	Discretisation
Clamped Reissner-Mindlin plate under uniform load	Linear shearable plate	MITC
Simply supported Reissner-Mindlin plate	Linear shearable plate	MITC
Clamped Reissner-Mindlin plate with MITC7	Linear shearable plate	MITC
Clamped Kirchhoff-Love plate	Linear unshearable plate	DG
Buckling of a heated von Kármán plate	Shearable weakly nonlinear plate	PSRI
Non-linear Naghdi roll-up cantilever	Nonlinear shearable shell	MITC
Clamped semi-cylindrical Naghdi shell under point load	Nonlinear shearable shell	PSRI
Partly Clamped Hyperbolic Paraboloid	Linear shearable shell	PSRI

Table 1: Structural models and discretisation techniques presented in main documented demos provided in FEniCS-Shells [39]. All the demos adopt shareable shell theory, except the *Clamped Kirchhoff-Love plate* which is based on the discontinuous Galerkin discretisation technique presented in [95, 74], not discussed in the present paper. All the combinations of models and discretisations are in principle possible, although we obtained better results using the proposed MITC implementation for linear plates and PSRI for linear and nonlinear shells.

2. Structural models

This section presents the variational formulation of the equilibrium problem for the basic plate and shell models considered in this work. Starting from the most general model, the *nonlinear Naghdi shell model* [71], the linear *Reissner-Mindlin plate model* [80, 70] is obtained as a special case of the *linear Naghdi shell model* [72]. In passing, we present also the so-called *Marguerre-von Kármán shallow shell model* [67], because (in its unshearable version) it is extensively used in the literature to study nonlinear phenomena in plates and shallow shells [65, 58, 12]. We review below the basic notations used in this work.

Notation. We equip the Euclidean space with a Cartesian frame $\{O; a_1, \dots, a_n\}$ with orthogonal unit basis vectors $a_i \in \mathcal{V}^n$, $\mathcal{V}^n$ being the translation space. Let $x = X - O \in \mathcal{V}^n$ denote the position vector of the point X whose rectangular Cartesian coordinates are $(X_1, \dots, X_n) \in \mathbb{R}^n$. We denote by $\mathbb{R}^{m\times n}$ the space of $m \times n$ matrices and by $\mathbb{S}^n = \{S \in \mathbb{R}^{n\times n} : S = S^T\}$ the space of symmetric $n \times n$ matrices, $\mathbb{S}^n_+$ its subset of positive definite matrices. With a notational abuse, for any tensor field $T \in \mathcal{V}^n \otimes \cdots \otimes \mathcal{V}^n$, let $T \in \mathbb{R}^{n\times\cdots\times n}$ denote also the collection of its Cartesian components. The same applies to vectors and tensors on manifolds. We denote by $a \cdot$ the inner product between two tensors. In particular if T is a tensor of order $2n$ and v a tensor of order n, we denote by Tv the application of the tensor T on v and by $Tv \cdot v$ the quadratic form on the space of v having T as metric. For $v \in \mathbb{R}^n$ and $x \in \mathbb{R}^m$, $\nabla v \in \mathbb{R}^{n\times m}$ denotes the linear operator such that $\mathrm{d}v = \nabla v\, \mathrm{d}x + o(|\mathrm{d}x|^2)$. We often use also index notation, where Latin indices (*e.g.* i, j) are assumed to take the values $1, 2, 3$, whilst Greek indices (*e.g.* α, β) take the values $1, 2$. For the partial derivatives of a function f we use the abridged notation $f_{,\alpha} = \partial f/\partial x_\alpha$. We define the space $L^2(\omega)$ as the usual Sobolev space of square-integrable functions on the domain ω with respect to the Lebesgue measure $\mathrm{d}x$. Then $H^s(\omega)$ is the usual Sobolev space of $L^2(\omega)$ functions whose weak derivatives of order $s \in \mathbb{N}$ are also in $L^2(\omega)$. We use the notation $f \in H^s(\omega; \mathbb{R}^n)$ to denote a vector-valued function whose components $(f_1, \cdots, f_n)$ are each functions in $H^s(\omega)$.

2.1. Non-linear Naghdi shell model

Kinematics. We describe the reference configuration of *shell-like* bodies as:

$$p_0(x_\alpha, x_3) = \phi_0(x_\alpha) + x_3\, n_0(x_\alpha)\,, \qquad x_\alpha \in \omega \subset \mathbb{R}^2, \quad x_3 \in [-t/2, t/2],$$

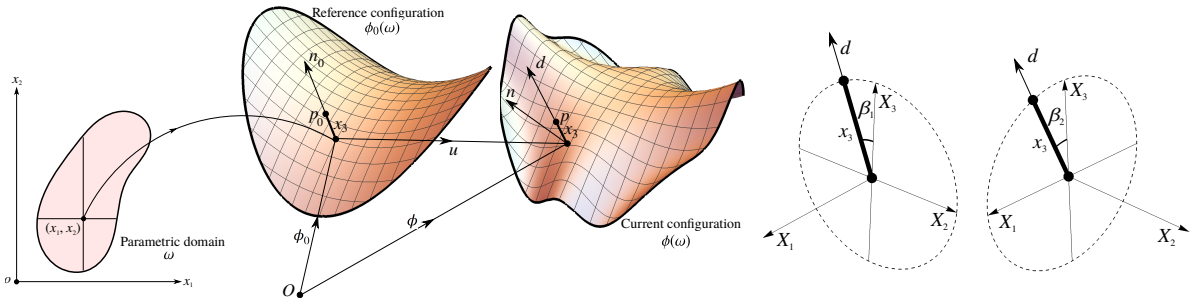

Figure 1: Kinematics of the nonlinear Naghdi shell model. Left: Parametric domain ω and placement of a generic point of the shell in the reference and current configuration. Right: Parameterisation of the director d in terms of the β_1, β_2 angles.

where (x_α, x_3) are curvilinear coordinates, $\phi_0 : \omega \to \mathbb{R}^3$ is a (piece of) regular surface, and $n_0 = (\partial_1\phi_0 \times \partial_2\phi_0)/\left|\partial_1\phi_0 \times \partial_2\phi_0\right|$ ($\times$ refers to the vector cross-product in only this context) is a continuous unit vector field normal to the middle surface $\phi_0(\omega)$, Fig. 1.

The vectors $g_{0,\alpha} = \partial_\alpha\phi_0$ define a covariant basis on the tangent plane at each point of the reference configuration. The slenderness condition requires the thickness t to be much smaller that the diameter of the middle surface ω. The geometry of the middle surface is completely described by the metric and curvature tensors, a_0 and b_0 respectively, whose covariant components are computed as:

$$a_0 = \nabla\phi_0^T\nabla\phi_0, \qquad b_0 = -\frac{1}{2}\big(\nabla\phi_0^T\nabla n_0 + \nabla n_0^T\nabla\phi_0\big), \qquad a_0 \in \mathbb{S}^2_+,\, b_0 \in \mathbb{S}^2,$$

where $\nabla\phi_0 = [g_{0,1}, g_{0,2}]$. Whenever the reference configuration is chosen to be flat, that is when $\phi_0(\omega)$ is a planar surface, $n_0 \equiv a_3$ (and $x_3 \equiv X_3$) and $b_0 = 0$. In such a case a body is said *plate-like*.

In the nonlinear Naghdi shell model the current configuration of the shell is written as a sum of the placement of the middle surface $\phi : \omega \to \mathbb{R}^3$ (or alternatively the displacement field $u = \phi - \phi_0$) and of the director field $d : \omega \to \mathbb{R}^3$ (see Figure 1):

$$p(x_\alpha, x_3) = \phi(x_\alpha) + x_3\, d(x_\alpha).$$

In general, $|d| \neq 1$ and $d \cdot n \neq 0$, where $n = (\partial_1\phi \times \partial_2\phi)/\left|\partial_1\phi \times \partial_2\phi\right|$ is the unit normal to the current surface and the vectors $g_\alpha = \partial_\alpha\phi$ define a covariant basis on the tangent plane at each point of the deformed configuration. When the normal fibres are assumed to be unstretchable, $|d| = 1$ and the director can be parametrised by two angles $\beta = (\beta_1, \beta_2) : \omega \to \mathbb{R}^2$, e.g., $d(\beta) = (\cos\beta_1 \sin\beta_2, -\sin\beta_1, \cos\beta_1\cos\beta_2)$, giving rise the so-called five-parameter shell model [21] (the three-components of the displacement field and the two angles (β_1, β_2)), Figure 1.

In a Lagrangian description, we use the following measures of deformation for the shell [71, 66]:

$$\begin{aligned} e_N(u) &= \frac{1}{2}\big(\nabla\phi(u)^T\nabla\phi(u) - a_0\big), \\ k_N(u,\beta) &= -\frac{1}{2}\big[\nabla\phi(u)^T\nabla d(\beta) + \nabla d(\beta)^T\nabla\phi(u)\big] - b_0, \\ \gamma_N(u,\beta) &= \nabla\phi(u)^T d(\beta), \end{aligned} \tag{1}$$

representing the stretching of the middle plane (a second order tensor), the bending curvature (a second order tensor), and the shear strain vector, respectively. The shear strain vanishes if and only if the director d coincides with the unit normal to the surface.

Strain energy and constitutive equations. We consider elastic shells characterised by an elastic strain energy density in the reference configuration $\hat{\psi}(e, k, \gamma)$, a scalar function of the deformations. The stress measures are the membrane stress resultant $N = \partial_e \hat{\psi}$, a second order tensor, the couple stress resultant $M = \partial_k \hat{\psi}$ a second order tensor, and the vector $T = \partial_\gamma \hat{\psi}$ representing the transverse shear stress. We will focus in our examples on linearly elastic constitutive behaviour for which the strain energy density is a quadratic function of the strain measures. Thus, using standard notation:

$$\hat{\psi}(e, k, \gamma) = \frac{1}{2} A(e - \bar{e}) \cdot (e - \bar{e}) + B(e - \bar{e}) \cdot (k - \bar{k}) + \frac{1}{2} D(k - \bar{k}) \cdot (k - \bar{k}) + \frac{1}{2} S\gamma \cdot \gamma,$$

where A, D are fourth-order and positive-definite tensors providing the membrane and bending stiffness, B is a fourth order tensor providing the membrane-to-bending constitutive coupling, S is a second order tensor providing the shear stiffness and $\bar{e}, \bar{k}$ are symmetric second order tensor fields representing inelastic stretching and bending strains. In what follows, unless otherwise stated, $\bar{e}, \bar{k} = 0$. This leads to the following linear constitutive laws:

$$N = A(e - \bar{e}) + B(k - \bar{k}), \qquad M = B(e - \bar{e}) + D(k - \bar{k}), \qquad T = S\gamma.$$

The stored energy density is the sum of membrane, $\hat{\psi}_m$, bending, $\hat{\psi}_b$, and shearing, $\hat{\psi}_s$, contributions:

$$\hat{\psi}(e, k, \gamma) = \hat{\psi}_m + \hat{\psi}_b + \hat{\psi}_s = \frac{1}{2} N \cdot (e - \bar{e}) + \frac{1}{2} M \cdot (k - \bar{k}) + \frac{1}{2} T \cdot \gamma.$$

For a shell made of a single homogeneous layer of St. Venant-Kirchhoff isotropic material the contravariant components of the elastic tensors are:

$$\frac{A^{\alpha\beta\sigma\tau}}{t} = 12\frac{D^{\alpha\beta\sigma\tau}}{t^3} = \frac{2\lambda\mu}{\lambda + 2\mu} a_0^{\alpha\beta} a_0^{\sigma\tau} + \mu \left(a_0^{\alpha\sigma} a_0^{\beta\tau} + a_0^{\alpha\tau} a_0^{\beta\sigma} \right), \quad B^{\alpha\beta\sigma\tau} = 0, \qquad S^{\alpha\beta} = \mu a_0^{\alpha\beta},$$

where $a_0^{\alpha\beta}$ are the contravariant components of the metric tensor a_0 and λ, μ the Lamé constants. Denoting by $\epsilon = t/L$ the small thinness parameter, $|A|, |S| \propto \epsilon$, while $|B| \propto \epsilon^2$ and $|D| \propto \epsilon^3$. *Pure bending deformations* ($e = 0$, $\gamma = 0$) are energetically cheaper and, whenever possible, they are preferred.

Variational formulation of the equilibrium condition. We focus here on the solution of quasi-static problems under the action of conservative loads, although this is not a limitation of the FEniCS-Shells library. The equilibrium configurations are found by solving for the stationary points of the potential energy:

$$\mathit{\Pi}_N(u, \beta) = \int_\omega \hat{\psi}(e_N(u), k_N(u, \beta), \gamma_N(u, \beta)) \sqrt{j_0} \, \mathrm{d}x - W_{\text{ext}}, \tag{2}$$

where W_{ext} is the external work of the conservative forces and $j_0 = \det a_0$. Considering as Dirichlet boundary conditions imposed displacements $\bar{u}$ on the part of the boundary γ_u and on the rotation $\bar{\beta}$ on γ_β, the space of admissible displacements and rotations are, respectively:

$$\mathcal{U} \equiv \{u \in H^1(\omega, \mathbb{R}^3) \,|\, u = \bar{u} \text{ on } \gamma_u\}, \quad \mathcal{R} \equiv \{\beta \in H^1(\omega, \mathbb{R}^2) \,|\, \beta = \bar{\beta} \text{ on } \gamma_\beta\}. \tag{3}$$

The variational formulation of the equilibrium equation consist in finding $(u, \beta) \in \mathcal{U} \times \mathcal{R}$ such that

$$D_{\tilde{u}} \left[\mathit{\Pi}_N(u, \beta) \right] = 0, \quad D_{\tilde{\beta}} \left[\mathit{\Pi}_N(u, \beta) \right] = 0, \quad \forall (\tilde{u}, \tilde{\beta}) \in \mathcal{U}_0 \times \mathcal{R}_0, \tag{4}$$

where $\mathcal{U}_0$ and $\mathcal{R}_0$ are the vector spaces associated to $\mathcal{U}$ and $\mathcal{R}$, obtained by setting $\bar{u} = 0$ and $\bar{\beta} = 0$ in (3). The stability of an equilibrium can by assessed by studying the sign of the second derivative of the energy, a quadratic form of the variations $\tilde{u}$, $\tilde{\beta}$.

Remark. *Shell models with energy in the form* (2) *are* shearable*, since flexure is due to both bending and shearing. However, for very thin shells and plates the shearing strains turn out to be negligible. These structures are quite naturally modelled by means of* unshearable *or* pure bending *theories obtained by imposing the inner constraint* $\gamma = 0$*. Such theories can usually be recovered as limit models of shearable theories when the thinness parameter goes to zero,* $\epsilon \to 0$*. In what follows the shell models in the library are introduced in their 'shearable version'; their unshearable counterpart can be easily derived. We remark that the distinction between shearable and unshearable theories is of paramount importance, since the numerical solution procedures exhibit quite different challenges.*

Remark. *By assuming the inner constraint* $\gamma_N = 0$*, from Eq.* $(1)_3$ $d = n \in \ker \nabla\phi^T(u)$*. Moreover, from Eq.* $(1)_2$*, the change of curvature can be written as* $k(u) = b(u) - b_0$*,* $b(u)$ *being the curvature tensor of the current surface. In such a way the nonlinear* Koiter shell model *[54] is recovered as the unshearable counterpart of the Naghdi's one for thin shells. Since* $b_{\alpha\beta} = n_{i,\beta}\,(\phi_0 + u)_{,\alpha} = n_i\,(\phi_0 + u)_{,\alpha\beta}$*,* $(i = 1, 2, 3)$*, the displacement* u *must be sought in a space* $\mathcal{U} \subseteq H^2(\omega, \mathbb{R}^3)$*. This high regularity requirement is a common feature of the unshearable theories.*

2.2. Marguerre-von Kármán shallow shell model

Some widely studied and used weakly non-linear versions of the Naghdi shell equations are the *Föppl-von Kármán plate model* [37, 94] and the *Marguerre shallow shell model* [67]. They can be seen as the simplest nonlinear models able to properly describe the moderately large deflections of thin shallow shells or plates, since they retain a minimal geometrical coupling between the membrane and flexural behaviour. Here, we introduce them in their shearable version [48].

Consider a shell with a *shallow* initial configuration $\phi_0(x_\alpha) = x_\alpha\, a_\alpha + \zeta(x_\alpha)a_3$, with the shallowness assumption $|\nabla\zeta| \sim \eta \ll 1$ and let $\phi(x_\alpha) = x_\alpha a_\alpha + v(x_\alpha) + w(x_\alpha)a_3$ be the current configuration, where e_3 of the middle plane with respect to a flat configuration $x = x_\alpha e_\alpha \in \omega$, and decompose the $v \perp \omega$ is the in-plane component and w on the $a_1 - a_2$ plane, with $v \cdot a_3 = 0$, and the transverse component wa_3. Similarly, we denote by θ the (small) rotations of the fibres orthogonal to the middle-plane, with $\theta \cdot a_3 = 0$.

The displacement of an arbitrary point of the three-dimensional body can be represented as:

$$U_M(x_\alpha, x_3) = v(x_\alpha) + w(x_\alpha)a_3 - x_3\,\theta(x_\alpha). \tag{5}$$

The *Marguerre-von Kármán shallow shell model* can be derived from the nonlinear Naghdi model by assuming $|v|/L \sim \eta^2$, $|w|/L \sim \eta$ and $|\theta| \sim \eta$, so that $d(x_\alpha) - n_0(x_\alpha) = \theta(x_\alpha) + \text{h.o.t.}$, where $\theta(x_\alpha) = \beta(x_\alpha) \times a_3$. Then, the Marguerre-von Kármán strain measures are obtained as the leading order terms of the Naghdi strain measures, Eqs. 1,

$$\begin{aligned} e_M(v, w) &= \frac{\nabla v + \nabla v^T}{2} + \frac{\nabla w \otimes \nabla w}{2} - \frac{\nabla\zeta \otimes \nabla\zeta}{2}, \\ k_M(\theta) &= \frac{\nabla\theta + \nabla\theta^T}{2} - \nabla\nabla\zeta, \qquad \gamma_M(w, \theta) = \nabla w - \theta. \end{aligned} \tag{6}$$

Then, solutions are found as the minimisers over a smooth set of vector fields $v \in \mathcal{V} \subseteq H^1(\omega, \mathbb{R}^2)$, $w \in \mathcal{W} \subseteq H^1(\omega)$, $\theta \in \mathcal{R} \subseteq H^1(\omega, \mathbb{R}^2)$ satisfying appropriate boundary conditions, of the nonlinear

Marguerre-von Kármán energy functional:

$$\Pi_M(v,w,\theta) = \frac{1}{2}\int_\omega N_M(v,w)\cdot\big(e_M(v,w)-\bar{e}\big)\,\mathrm{d}x + \frac{1}{2}\int_\omega M_M(w,\theta)\cdot\big(k_M(w,\theta)-\bar{k}\big)\,\mathrm{d}x + \frac{1}{2}\int_\omega T_M(w,\theta)\cdot\gamma_M(w,\theta)\,\mathrm{d}x - W_{\text{ext}}. \quad (7)$$

Remark. *By assuming the inner constraint $\gamma_M = 0$, from Eq. $(6)_3$, $\theta = \nabla w$. Moreover, from Eq. $(6)_2$, $k(w) = \nabla\nabla w$. In such a way the classical (unshearable) Marguerre-von Kármán shallow shell model is recovered. As for the Koiter model [54], the transverse displacement w must be sought in a space $\mathcal{W} \subseteq H^2(\omega)$.*

2.3. Linear Naghdi shell model

Consider a shell body with reference surface $\phi_0(\omega)$. Again, let $U_{\tilde{N}}(x_\alpha, x_3) = u(x_\alpha)a_3 - x_3\,\theta(x_\alpha)$ be the representation formula for the displacement vector field, with $\theta \in T_P\,\phi_0(x_\alpha)$, $T_P\,\phi_0(x_\alpha)$ being the tangent plane to the reference surface at the point $\phi_0(x_\alpha)$; u represents an (infinitesimal) displacement from the reference surface, θ denotes the (infinitesimal) rotation of the fibers orthogonal to the middle surface. The *linear* Naghdi strain measures are then obtained by linearisation from Eqs. (1),

$$\begin{aligned} e_{\tilde{N}}(u) &= \frac{1}{2}\big(\nabla\phi_0^T\nabla u + \nabla u^T\nabla\phi_0\big),\\ k_{\tilde{N}}(u,\theta) &= -\frac{1}{2}\big(\nabla{\phi_0}^T\nabla\theta + \nabla\theta^T\nabla\phi_0\big) - \frac{1}{2}\big(\nabla{n_0}^T\nabla u + \nabla u^T\nabla n_0\big),\\ \gamma_{\tilde{N}}(u,\theta) &= \nabla{\phi_0}^T\theta + \nabla u^T n_0. \end{aligned} \quad (8)$$

Then, solutions are found as the minimisers over a smooth set of vector fields $u \in \mathcal{U} \subseteq H^1(\omega,\mathbb{R}^3)$, $\theta \in \mathcal{R} \subseteq H^1(\omega,\mathbb{R}^2)$ satisfying appropriate boundary conditions, of the linear Naghdi energy functional:

$$\Pi_{\tilde{N}}(u,\theta) = \frac{1}{2}\int_\omega N_{\tilde{N}}(u)\cdot e_{\tilde{N}}(u)\,\mathrm{d}x + \frac{1}{2}\int_\omega M_{\tilde{N}}(u,\theta)\cdot k_{\tilde{N}}(u,\theta)\,\mathrm{d}x + \frac{1}{2}\int_\omega T_{\tilde{N}}(u,\theta)\cdot\gamma_{\tilde{N}}(u,\theta)\,\mathrm{d}x - W_{\text{ext}}. \quad (9)$$

Remark. *For a plate-like body, Eqs. (8) reduce to:*

$$e_{RM}(v) = \frac{1}{2}\big(\nabla v + \nabla v^T\big), \qquad k_{RM}(v,\theta) = \frac{1}{2}\big(\nabla\theta + \nabla\theta^T\big), \qquad \gamma_{RM}(w,\theta) = \nabla w - \theta, \quad (10)$$

where $u(x_\alpha) = v(x_\alpha) + w(x_\alpha)\,a_3$. In such a case the membrane and flexural problem are geometrically decoupled and a linear coupling turns out to be possible only at the constitutive level. Eqs. $(10)_{2,3}$ are the Reissner-Mindlin plate strain measures, depending only by the transverse displacement w and the rotation θ. Again, solutions are found as the minimisers over a smooth set of vector fields $w \in \mathcal{W} \subseteq H^1(\omega)$, $\theta \in \mathcal{R} \subseteq H^1(\omega,\mathbb{R}^2)$, satisfying appropriate boundary conditions, of the Reissner-Mindlin energy functional:

$$\Pi_{RM}(w,\theta) = \frac{1}{2}\int_\omega M_{RM}(w,\theta)\cdot k_{RM}(w,\theta)\,\mathrm{d}x + \frac{1}{2}\int_\omega T_{RM}(w,\theta)\cdot\gamma_{RM}(w,\theta)\,\mathrm{d}x - W_{ext}. \quad (11)$$

Remark. *By assuming the inner constraints $\gamma_{\tilde{N}} = 0$ and $\gamma_{RM} = 0$, the linear* Koiter shell model *[55] and the Kirchhoff-Love [51, 62] plate model are recovered, respectively. Solutions of such unshearable models must be sought in spaces $\mathcal{U} \subseteq H^2(\omega,\mathbb{R}^3)$, $\mathcal{W} \subseteq H^2(\omega)$, respectively.*

3. Finite element formulations and implementation details

Notation. We use nomenclature from [60] related to finite element methods. We let $\mathcal{T}_h$ (the mesh) be a partition of the domain ω into a finite set of triangular cells $\mathcal{T}_h = \{T\}$ with disjoint interiors:

$$\cup_{T\in\mathcal{T}_h} T = \omega.$$

Each triangular cell T has circumradius h_T, and $h := \max_{T\in\mathcal{T}_h} h_T$. We then denote the set of edges of T_h as $\mathcal{E} = \{E\}$. $\mathcal{E}_h^{\text{int}} \subset \mathcal{E}_h$ is the subset of edges on the interior of the mesh (i.e. not on the boundary). Normals to the edges of each cell are denoted n. Functions u evaluated on opposite sides of an edge E are indicated by the subscripts $+$ and $-$, giving the jump operator $[\![u]\!] = u_+ \cdot n_+ + u_- \cdot n_-$. We denote $CG_p \subset H^1(\omega)$ the standard continuous Lagrangian finite element space of polynomial order p constructed on the mesh $\mathcal{T}_h$. The notation $f \in [CG_p]^n \subset H^s(\omega; \mathbb{R}^n)$ denotes a vector-valued function whose components $(f_1, \cdots, f_n)$ are each a member of CG_p.

3.1. Background

As pointed out in the previous section, shearable models give rise to weak formulations with solutions in H^1 while unshearable models give rise to weak formulations with solutions in H^2. It is well-known that producing conforming finite element method discretisations of H^2 is not straightforward, although several elegant solutions are possible [32, 74, 20, 42]. To bypass this issue, one can choose to use shearable models even for very thin structures, even though in such cases shear strains are negligible. Shearable models only requires H^1-conforming finite element methods which are significantly easier to implement than either discontinuous Galerkin or H^2-conforming finite element methods.

Unfortunately it is also the case that applying standard H^1 conforming finite element methods leads to *shear-locking* in the thin limit, since the finite element spaces are unable to properly represent the zero shear-strain $\gamma = 0$ constraint asymptotically enforced within the mathematical model as the thinness parameter goes to zero. A similar problem arises in shell problems whenever pure bending displacements are non-inhibited: H^1 conforming finite element methods for such *bending-dominated* shells suffer of *membrane-locking* [28, 86, 87]. In other words, the discrete spaces are incompatible with the structural models.

A wide variety of locking-free numerical methods exist, including the methods of assumed natural strains [16, 29, 47], enhanced assumed strains [91, 22], discrete shear gap [23], partial selective reduced integration [9] and mixed variational [42] approaches have been developed to overcome this problem. Implementing these locking-free approaches is more complex than implementing the standard H^1-conforming finite element method as they require mixed formulations and special finite element function spaces. Making these methods easier to code, use and adapt is one of the main goals of the present work and the companion open-source library FEniCS-Shells.

For alleviating shear-locking in the Reissner-Mindlin and Marguerre-von Kármán models we have chosen to implement a Mixed Interpolation Tensorial Components (MITC) reduction operator. The MITC approach was introduced in the paper of Bathe and Dvorkin [15] for curing shear-locking in the finite element discretisation of the Reissner-Mindlin model. Other notable contributions along the same lines include the Durán-Liberman [35] and the MITC7 and MITC9 [16] elements. The success of the various MITC elements for the Reissner-Mindlin problem rests on solid results in numerical analysis, e.g. [16, 3]. It has also been shown numerically that MITC approach can be successful in solving membrane and shear locking issues in the linear and non-linear Naghdi shell

models [47], although without rigorous mathematical justification. A fully general shell element with guaranteed mathematical and numerical behaviour in membrane and bending-dominated regimes is still out of reach and mathematically robust finite element design for shells is an active research topic. We have chosen to implement a high-order partial selective reduced integration (PSRI) method which was analysed for the linear Naghdi model in [9].

3.2. The shear and membrane-locking issues

For notational convenience we drop the explicit RM suffix relating to the Reissner-Mindlin model in what follows. Informally, when considering the Reissner-Mindlin plate model, shear-locking is the result of the Kirchhoff constraint (vanishing shear strain γ) [41]:

$$\gamma = \nabla w - \theta = 0, \tag{12}$$

being enforced on the discrete finite element spaces $w_h \in \mathcal{W}_h \subset \mathcal{W}$ and $\theta_h \in \mathcal{R}_h \subset \mathcal{R}$ for as the small thinness parameter $\epsilon \to 0$. The approximation power in the discrete finite element basis is inadequate to simultaneously represent the Kirchhoff (bending) dominated mode and also provide a uniformly convergent approximation to the problem with respect to ϵ.

More formally, denoting the continuous space of pure bending displacements ($\epsilon = 0$) as:

$$\mathcal{V}_0 = \{(w, \theta) \in \mathcal{W} \times \mathcal{R} \mid \nabla w - \theta = 0\}, \tag{13}$$

and the discrete solution $(w_h, \theta_h) \in \mathcal{V}_h := \mathcal{W}_h \times \mathcal{R}_h$, we seek solutions in a subspace $\mathcal{V}_{h0} \subset (\mathcal{V}_h \cap \mathcal{V}_0)$ containing discrete pure bending displacements:

$$\mathcal{V}_{h0} = \{(w_h, \theta_h) \in \mathcal{W}_h \times \mathcal{R}_h \mid \nabla w_h - \theta_h = 0\}. \tag{14}$$

It is not so hard to construct discretisations in which this requirement is quite catastrophic. Consider using standard $H^1(\omega)$-conforming linear Lagrangian elements for both fields, $\mathcal{W}_h := \mathrm{CG}_1$ and $\mathcal{R}_h := [\mathrm{CG}_1]^2$, and suppose fully clamped Dirichlet conditions on all of the boundary, that is $\mathcal{W}_h \subset H^1_0(\omega)$ and $\mathcal{R}_h \subset H^1_0(\omega, \mathbb{R}^2)$. With piecewise linear functions for w_h, ∇w_h then consists of piecewise constant functions. Furthermore, as θ_h must be zero on the boundary, and we are searching for solutions in the space $\mathcal{V}_{h0}$ where $\nabla w_h = \theta_h$, the only possible solution that our discrete space can represent is $w_h = 0$ and $\theta_h = 0$. The finite element model is overly stiff, hence the term 'locking'.

The membrane-locking issue arises in the linear and non-linear Naghdi shell models and the Marguerre-von Kármán shallow shell model. The locking issue can be motivated by a similar argument to the shear-locking issue and causes similarly poor results. However, the precise circumstances under which membrane-locking can appear is a more subtle matter, and can depend on a combination of geometry, boundary conditions and loading. We refer the reader to [28] for an excellent discussion of locking in shell finite element models. Here, we limit ourselves to remarks we consider strictly necessary to make our exposé understandable.

For simplicity in what follows, we refer to the linear Naghdi shell model. In this case, the continuous space of pure bending displacements (no membrane or shear strains) reads as:

$$\mathcal{V}_0 = \{(u, \theta) \in \mathcal{U} \times \mathcal{R} \mid e_N(u) = 0 \text{ and } \gamma_N(u, \theta) = 0\}. \tag{15}$$

When the thinness parameter goes to zero two distinct asymptotic behaviours emerge, depending on whether $\mathcal{V}_0$ is empty or not, and thus on the shape of the shell and the Dirichlet boundary

conditions applied on it. If $\mathcal{V}_0 = \emptyset$, pure bending is inhibited and the shell carries the load mainly by membrane actions; this is the so called *membrane-dominated regime*. Conversely, whenever $\mathcal{V}_0 \neq \emptyset$, pure bending is non-inhibited, the membrane and shearing contribution to the elastic energy vanish and the shell carries the load by bending actions; this is the so called *bending-dominated regime*. When considering finite element discretisations, this latter case is likely to suffer both membrane and shear locking, unless the discrete space $\mathcal{V}_{h0}$ is chosen so as to properly approximate the space $\mathcal{V}_0$ of pure bending displacements. In any case, since a finite element formulation should perform well regardless of the asymptotic regime, benchmark tests have to be provided for both membrane- and bending-dominated shells.

3.3. Mixed Interpolation of Tensorial Components (MITC) method

We use the MITC approach to deal with the shear-locking issue. The MITC approach is based on an underlying mixed variational method, where the Reissner-Mindlin shear strains γ are considered as an independent variable. One of the most attractive aspects of the MITC approach is that the final linear system of equations only contains the original primal unknown fields (w_h, θ_h) despite the consideration of the shear strain field γ_h in the formulation.

The first step in constructing an MITC-type element is the correct identification of the function space $\mathcal{S}(\omega; \mathbb{R}^2)$ in which the shear strain γ lives. For any scalar field $w \in H^1(\omega)$ it holds that $\nabla w \in H(\mathrm{rot}; \omega)$ where $H(\mathrm{rot}; \omega)$ is the Sobolev space of square-integrable vector-valued functions with square-integrable rot:

$$H(\mathrm{rot}; \omega) := \left\{ \gamma \in L^2(\omega; \mathbb{R}^2) \mid \mathrm{rot}\, \gamma := \partial_1 \gamma_2 - \partial_2 \gamma_1 \in L^2(\omega) \right\}. \tag{16}$$

Furthermore, for $\theta \in H^1(\omega; \mathbb{R}^2)$ we have $\mathrm{rot}\, \theta \in L^2(\omega)$ and thus it follows that

$$\gamma = \nabla w - \theta \in \mathcal{S} \equiv H(\mathrm{rot}; \omega). \tag{17}$$

Note that the operator rot is synonymous with the operator curl in $\mathbb{R}^2$.

Finite element approximation spaces that satisfy $\mathcal{S}_h \subset \mathcal{S}$ consist of the well-known 'curl/rot-conforming' elements, namely the Nédélec [73] (or rotated Raviart-Thomas elements [79] in $\mathbb{R}^2$) of the first NED_1^n and second kind NED_2^n, and the Brezzi-Douglas-Fortin-Marini (BDFM^n) elements [26], where n is the element (polynomial) order. All of these finite element spaces are available for use in FEniCS [4, 59, 5]. We refer the reader to [60] for a full description of the mathematical construction of these elements, and [82] as a reference for the issues surrounding their implementation in FEniCS.

For brevity, we shown only the development of the Durán-Liberman element [35]. This element can be considered the lowest order MITC-type element with rigorous analytical convergence proofs. There is also an implementation of MITC7 [16] in FEniCS-Shells but do not show the development in this paper.

The starting point is the discrete counterpart of eq. (11):

$$\begin{aligned} \Pi(w_h, \theta_h) &= \Pi^b(w_h, \theta_h) + \frac{1}{2} \int_\omega T(w_h, \theta_h) \cdot \gamma(w_h, \theta_h)\, \mathrm{d}x - W_{\mathrm{ext}}, \\ \Pi^b(w_h, \theta_h) &:= \frac{1}{2} \int_\omega M(w_h, \theta_h) \cdot k(w_h, \theta_h)\, \mathrm{d}x. \end{aligned} \tag{18}$$

The finite element spaces used in the construction of the Durán-Liberman element are continuous piecewise-linear Lagrangian elements for the transverse displacements $w_h \in \mathcal{W}_h := \mathrm{CG}_1$, continuous

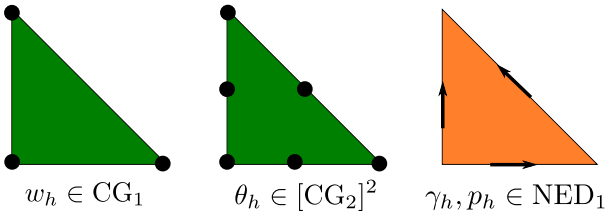

Figure 2: Finite element spaces making up the Durán-Liberman element. Circles denote point evaluations for degrees of freedom. Arrows denote point evaluations of tangential component for degrees of freedom. The Durán-Liberman has a total of 21 degrees of freedom: 3 for the displacement w_h, 12 for the rotations θ_h, 3 for the shear strain γ_h, and 3 for the Lagrange multiplier p_h. Thanks to the static condensation at the cell level, the latter 6 degrees of freedom for γ_h and p_h can be eliminated during the assembling process, reducing the number of effective degree of freedom per element to 15.

piecewise-quadratic vector-valued Lagrangian elements for the rotations $\theta_h \in \mathcal{R}_h := [\mathrm{CG}_2]^2$ and, finally, the lowest-order Nédélec elements of the first kind for the shear strain $\gamma_h \in \mathcal{S} := \mathrm{NED}_1$[1]. The product of these spaces then makes up the Durán-Liberman element, see Figure 2.

The element NED_1 is defined [60] by the Ciarlet triple $(T, \mathcal{V}, \mathcal{L})$ (cell, polynomial space, degrees of freedom):

$$T = \text{triangle}, \tag{19a}$$

$$\mathcal{V} = [\mathcal{P}_0(T)]^2 + \mathcal{S}_1(T), \tag{19b}$$

$$\mathcal{L} = \int_E v \cdot t\, p \,\mathrm{d}s, \text{ for } p \in \mathcal{P}_0(E),\ \forall E \subset T, \tag{19c}$$

where T is the reference triangle with edges E with measure $\mathrm{d}s$, $\mathcal{P}_0$ is the set of constant polynomial functions on the triangle T or edge E, and $\mathcal{S}_1(T)$ is the polynomial space:

$$\mathcal{S}_1(T) = \left\{ s \in [\mathcal{P}_1(T)]^2 \mid s(x) \cdot x = 0 \quad \forall x \in T \right\}. \tag{20}$$

The 'trick' of the MITC approach is recognising that by modifying the shear strain field at the discrete level by applying a special operator R_h that takes the primal to the conforming space $H(\mathrm{rot}; \omega)$ for the shear strains

$$R_h : \left[\mathrm{CG}_1 \times [\mathrm{CG}_2]^2\right] \to \mathrm{NED}_1 \tag{21}$$

the element can be 'unlocked'. For the Durán-Liberman element, the operator R_h can be defined by the following condition for each cell T in the mesh $\mathcal{T}_h$:

$$\int_E [(R_h[\gamma(w_h, \theta_h)] - \gamma_h) \cdot t]\, p \,\mathrm{d}s = 0, \forall p \in \mathcal{P}_0(E), \forall E. \tag{22}$$

[1] The original element construction of Durán and Liberman uses a slightly smaller quadratic space constructed as a sum of linear polynomials and quadratic bubbles. As this space is not available in FEniCS we use the full quadratic space instead.

Note that (22) is very similar to the degree of freedom definition $\mathcal{L}$ in (19c). In effect, R_h 'ties' the degrees of freedom of the transverse displacement and rotation space $CG_1 \times [CG_2]^2$ to an underlying NED_1 space. Then, applying the operator R_h to (18) gives:

$$\Pi(w_h, \theta_h) = \Pi^b(w_h, \theta_h) + \frac{1}{2}\int_\omega T(R_h\gamma(w_h, \theta_h)) \cdot R_h\gamma(w_h, \theta_h)\,\mathrm{d}x - W_{\text{ext}}. \tag{23}$$

Remark. *For the Reissner-Mindlin strain measure* $R_h\left[\gamma(w_h, \theta_h)\right] = \nabla w_h - R_h\theta_h$ *because* $R_h w_h = w_h$ *by definition. This application of the reduction operator to the rotation field is often found in the literature. However, in our work we always apply the reduction operator to the complete shear-strain variable* γ*.*

3.4. New implementation of the MITC method in FEniCS-Shells

The formulation and implementation of MITC in FEniCS-Shells is slightly different to the standard approach. In our view it is simpler to understand as it is purely variational and extends the MITC shear-locking cure quite naturally to the non-linear models. Another key advantage is that it can be concisely expressed in UFL [5].

Starting with (18) and this time directly substituting in the conforming strain field $\gamma_h \in \mathcal{S}_h$ gives:

$$\Pi(w_h, \theta_h, \gamma_h) = \Pi^b(w_h, \theta_h) + \int_\omega T(\gamma_h) \cdot \gamma_h\,\mathrm{d}x - W_{\text{ext}}. \tag{24}$$

We then 'tie' the tangential component of the conforming strain field $\gamma_h \cdot t$ to its counterpart calculated using the primal unknowns $\gamma \cdot t \equiv (\nabla w - \theta) \cdot t$ using a Lagrange multiplier field $p_h \in \text{NED}_1$ that lives on all edges $E \in \mathcal{E}_h$ of the mesh $\mathcal{T}_h$:

$$\Pi(w_h, \theta_h, \gamma_h, p_h) = \Pi^b(w_h, \theta_h) + \int_\omega T(\gamma_h)\cdot\gamma_h\,\mathrm{d}x + \sum_{E\in\mathcal{E}_h}\int_E (\gamma(w_h, \theta_h)\cdot t - \gamma_h\cdot t)\cdot(p_h\cdot t)\,\mathrm{d}s - W_{\text{ext}}. \tag{25}$$

It is possible to implement the Durán-Liberman element in FEniCS by directly expressing (25) using UFL. However, this comes at the expense of two extra fields γ_h and p_h over the standard MITC implementation.

Fortunately it is possible to eliminate both γ_h and p_h at the cell-local level. To this end, we begin by defining the residual $F(q; \tilde{q}) = 0$ as the usual Gâteaux derivative of (25) at a point $q_h := (w_h, \theta_h, \gamma_h, p_h)$ in the direction of test functions $\tilde{q} := (\tilde{w}, \tilde{\theta}, \tilde{\gamma}, \tilde{p})$:

$$F(q_h; \tilde{q}) := D_{\tilde{q}}\left[\Pi(q_h)\right] = 0, \qquad \forall \tilde{q} \in \text{CG}_1 \times [\text{CG}_2]^2 \times \text{NED}_1 \times \text{NED}_1, \tag{26}$$

which gives:

$$F(q_h; \tilde{q}) = a^b(w_h, \theta_h; \tilde{w}, \tilde{\theta}) + a^s(\gamma_h; \tilde{\gamma}) + a^{\Pi_h}(w_h, \theta_h, p_h; \tilde{\gamma}) + a^{\Pi_h}(\gamma_h; \tilde{w}, \tilde{\theta}, \tilde{p}) - W_{\text{ext}}(\tilde{q}) = 0, \tag{27a}$$

where:

$$a^b(w_h, \theta_h; \tilde{w}, \tilde{\theta}) = \int_\omega M(w_h, \theta_h) \cdot k(\tilde{w}, \tilde{\theta})\,\mathrm{d}x, \tag{27b}$$

$$a^s(\gamma_h; \tilde{\gamma}) = \int_\omega T(\gamma_h) \cdot \tilde{\gamma}\,\mathrm{d}x, \tag{27c}$$

$$a^{\Pi_h}(w_h, \theta_h, \gamma_h; \tilde{p}) = \sum_{E\in\mathcal{E}_h}\int_E (\gamma(w_h, \theta_h) \cdot t - \gamma_h \cdot t) \cdot (\tilde{p} \cdot t)\,\mathrm{d}s. \tag{27d}$$

Deriving the Jacobian involves taking the Gâteaux derivative again, this time at a point q_h in the direction of trial functions $q := (w, \theta, \gamma, p)$:

$$J(q_h; q; \tilde{q}) = D_q \left[F(q_h; \tilde{q}) \right]. \tag{28}$$

Because the Reissner-Mindlin equations are linear, this operation is trivial, giving:

$$J(q_h; q; \tilde{q}) = a^b(w, \theta; \tilde{w}, \tilde{\theta}) + a^s(\gamma; \tilde{\gamma}) + a^{\Pi_h}(w, \theta, p; \tilde{\gamma}) + a^{\Pi_h}(\gamma; \tilde{w}, \tilde{\theta}, \tilde{p}). \tag{29}$$

Using a standard Newton method, given an initial guess q^0 we seek for $k = 0, \ldots, n$ solutions $\delta q := (\delta w, \delta\theta, \delta\gamma, \delta p)$ to the linear systems:

$$J(q^k; q; \tilde{q})\, \delta q = -F(q^k; \tilde{q}), \tag{30}$$

$$q^{k+1} = q^k + \delta q. \tag{31}$$

The left and right-hand side of the discrete Newton linear system corresponding to (29) and (27) respectively, has the following block structure:

$$\begin{bmatrix} A & 0 & C \\ 0 & B & D \\ C^T & D & 0 \end{bmatrix} \begin{bmatrix} \delta z \\ \delta\gamma \\ \delta p \end{bmatrix} = \begin{bmatrix} b_z \\ b_\gamma \\ b_p \end{bmatrix}, \tag{32}$$

where $\delta z := (\delta w, \delta\theta)$ and A, B correspond to the matrices associated with bilinear forms a^b and a^s in (29), respectively. The matrix D is a diagonal-form edge mass matrix arising from the bilinear form:

$$-\sum_{E \in \mathcal{E}_h} \int_E (\gamma \cdot t) \cdot (\tilde{p} \cdot t)\, \mathrm{d}s, \tag{33}$$

and C arises from the bilinear form:

$$\sum_{E \in \mathcal{E}_h} \int_E (\gamma(w_h, \theta_h) \cdot t) \cdot (\tilde{p} \cdot t)\, \mathrm{d}s. \tag{34}$$

The notation $b_{(.)}$ corresponds to a splitting of the residual vector into its sub-blocks on the functions z, γ and p.

Solving for $\delta\gamma$ with row two of (32):

$$\delta p = D^{-1}(b_\gamma - B\delta\gamma), \tag{35}$$

and for $\delta\gamma$ with row three of (32)

$$\delta\gamma = D^{-1}(b_p - C^T\delta z), \tag{36}$$

and then eliminating $\delta\gamma$ from (35) using: (36) gives

$$\delta p = D^{-1}(b_\gamma - BD^{-1}b_p + BD^{-1}C^T\delta z), \tag{37}$$

before finally eliminating δp from the first row of (32) using (37) and rearranging to give:

$$A_s\delta z = b_s, \tag{38a}$$

$$A_s = (A + CD^{-1}BD^{-1}C^T), \tag{38b}$$

$$b_s = b_z + CD^{-1}BD^{-1}b_p - CD^{-1}b_\gamma. \tag{38c}$$

```
1  from dolfin import *; import fenics_shells as fs; import matplotlib.pyplot as plt
2  mesh = UnitSquareMesh(32, 32)
3  # Duran-Liberman element
4  element = MixedElement([VectorElement("Lagrange", triangle, 2), # rotations (theta)
5                          FiniteElement("Lagrange", triangle, 1), # displacement (w)
6                          FiniteElement("N1curl", triangle, 1), # reduced shear strain (R_gamma)
7                          FiniteElement("N1curl", triangle, 1)]) # Lagrange multiplier (p)
8  # Special projected function space (this is defined in fenics-shells)
9  Q = fs.ProjectedFunctionSpace(mesh, element, num_projected_subspaces=2)
10 Q_F = Q.full_space # Full function space for the mixed variational formulation
11 # Definitions for the variational formulations
12 q_, q, q_t = Function(Q_F), TrialFunction(Q_F), TestFunction(Q_F)
13 theta_, w_, R_gamma_, p_ = split(q_) # rotations, displacement, shear strain, Lagrange multipliers.
14 # Material properties
15 E = Constant(10920.0); nu = Constant(0.3); kappa = Constant(5.0/6.0); t = Constant(0.001)
16 D = (E*t**3)/(24.0*(1.0 - nu**2))
17 # Deformations
18 k = sym(grad(theta_)) # Curvature
19 gamma = grad(w_) - theta_ # Shear strain
20 # Duran-Liberman tying
21 Pi_R = fs.inner_e(gamma - R_gamma_, p_) # This is defined in fenics_shells
22 # Energy densities
23 psi_b = D*((1.0 - nu)*tr(k*k) + nu*(tr(k))**2) # Bending
24 psi_s = ((E*kappa*t)/(4.0*(1.0 + nu)))*inner(R_gamma_, R_gamma_) # Shear
25 # External work
26 f = Constant(1.0)
27 W_ext = inner(f*t**3, w_)*dx
28 # Mixed variational forms
29 Pi = psi_M*dx + psi_T*dx + Pi_R - W_ext # Energy
30 F = derivative(Pi, q_, q_t) # Residual
31 J = derivative(F, q_, q) # Jacobian
32 # Assemble the linear system: the special projected assembler returns a linear system
33 # in the primal variables (theta, w) eliminating the local variables (R_gamma_, p_)
34 A, b = fs.assemble(Q, J, -F)
35 bc = DirichletBC(Q, Constant((0.0, 0.0, 0.0)), "on_boundary")
36 bc.apply(A, b)
37 # Solve the linear system in the primal space (theta, w)
38 theta_w_ = Function(Q) # (theta, w)
39 solver = LUSolver("mumps") # Use a direct solver
40 solver.solve(A, theta_w_.vector(), b)
41 # Postprocessing
42 theta_sol, w_sol = theta_w_.split(deepcopy=True) # extract rotations and displacement
43 plot(w_sol, title = "Displacement"); plt.savefig("w.png"); plt.close();
44 plot(theta_sol, title = "Rotation"); plt.savefig("theta.png")
```

Figure 3: Complete Python code for solving clamped Reissner-Mindlin problem with uniform transverse loading.

Note again that D is diagonal and can thus be cheaply inverted at the cell-local level allowing (38) to be formed locally as well. The above procedure is implemented at the element level using a custom assembly function written in C++. FEniCS automatically returns the dense cell-local version of the block structured system (32) corresponding to the Jacobian (29) and residual (27) forms. We then use the Eigen dense linear algebra package [38] to split up (32) into its constituent blocks before calculating A_s and b_s using (38). The cell-local contributions A_s and b_s are then assembled into a sparse matrix and vector associated with global displacement unknowns δz only. Solving for the global unknown δz, we can then reconstruct the eliminated unknowns $\delta\gamma$ and δp by post-processing at the cell-local level using (36) and (35), respectively.

A Python code showing how to define the Reissner-Mindlin problem in FEniCS-Shells is given in Figure 3. The new `ProjectedFunctionSpace` class (line 9 in Figure 3) manages the relationship between full function space space with all unknowns $q_h := (w_h, \theta_h, \gamma_h, p_h)$ the reduced function space unknowns with displacement unknowns $z = (w_h, \theta_h)$. The special custom assembly procedure in FEniCS-Shells is invoked via a call to `assemble` passing the `ProjectedFunctionSpace` object as the first argument, resulting in the elimination of $\delta\gamma$ and δp at the local level (line 34 in Figure 3).

The above procedure applies directly to the case of models with non-linear strain measures, e.g.

the non-linear Naghdi shell model (see Section 2.1). The tying term in the Lagrangian is simply re-written using the appropriate strain measure γ_N:

$$\sum_{E\in\mathcal{E}_h}\int_E (\gamma_N(u_h,\beta_h)\cdot t-\gamma_{Nh}\cdot t)\cdot(p_h\cdot t)\,\mathrm{d}s, \tag{39}$$

before being consistently linearised at the symbolic level using the tools in UFL. The resulting discrete Newton system has precisely the same block form as (32), and so the same linear algebra assembly procedure can be used to eliminate the auxiliary unknowns γ_{Nh} and p_h. We refer the reader to the documented demo *Non-linear Naghdi roll-up cantilever* [39] for an example applying MITC to a non-linear shell problem. Note, however, that we explicitly cure here only shear locking. Our high-level approach makes it relatively straightforward to directly apply MITC to user-specified thin structural models.

3.5. Partial Selective Reduced Integration (PSRI)

We use the PSRI approach to simultaneously deal with the shear- and membrane-locking issues in the shell-like models. Our method is inspired by, but not identical to the one shown in [9], which contains convergence proofs for the linear Naghdi model. The PSRI approach can be viewed as a reduced integration method[9], a stabilised mixed method [30], or an augmented Lagrangian method [24].

Following [9] we begin with the discrete linear Naghdi energy functional:

$$\begin{aligned}\Pi_{\tilde{N}}(u,\theta)=\frac{1}{2}\int_\omega N_{\tilde{N}}(u_h)\cdot e_{\tilde{N}}(u_h)\,\mathrm{d}x+\frac{1}{2}\int_\omega M_{\tilde{N}}(u_h,\theta_h)\cdot k_{\tilde{N}}(u_h,\theta_h)\,\mathrm{d}x\\ +\frac{1}{2}\int_\omega T_{\tilde{N}}(u_h,\theta_h)\cdot\gamma_{\tilde{N}}(u_h,\theta_h)\,\mathrm{d}x-W_{\mathrm{ext}},\end{aligned} \tag{40}$$

or in shortened form:

$$\Pi_{\tilde{N}}(u,\theta)=\Pi^m(u_h)+\Pi^b(u_h,\theta_h)+\Pi^s(u_h,\theta_h)-W_{\mathrm{ext}}, \tag{41}$$

where $\Pi^m(u_h)$, $\Pi^b(u_h,\theta_h)$ and $\Pi^s(u_h,\theta_h)$ correspond to the membrane, bending and shear energies of the linear Naghdi model, respectively.

The finite element spaces used in the construction of the PSRI element are second-order continuous piecewise-quadratic cubic-bubble-enriched Lagrangian elements for the displacements $u_h\in\mathcal{U}_h:=[CG^2+B_3]^3$ and second-order continuous piecewise-quadratic Lagrangian elements for the rotations $\theta\in\mathcal{R}_h:=[CG^2]^2$. The finite element space of cubic bubbles B_3 is defined by the Ciarlet triple $(T,\mathcal{V},\mathcal{L})$:

$$T=\text{triangle},\qquad \mathcal{V}=\{v\in\mathcal{P}_3(T)\mid v|_E=0\},\qquad \mathcal{L}=v\,(1/3,1/3)\,. \tag{42}$$

We then introduce a parameter $\alpha\in\mathbb{R}$ that splits the membrane and shear energy in the energy functional into a weighted sum of two parts:

$$\Pi_{\tilde{N}}(u,\theta)=\Pi^b(u_h,\theta_h)+\alpha\Pi^m(u_h)+(1-\alpha)\Pi^m(u_h)+\alpha\Pi^s(u_h,\theta_h)+(1-\alpha)\Pi^s(u_h,\theta_h)-W_{\mathrm{ext}}, \tag{43}$$

to which we apply reduced integration to the parts weighted by the factor $1-\alpha$. As discussed in [9] a more refined interpretation of PSRI is a stabilised mixed formulation where the extra stress

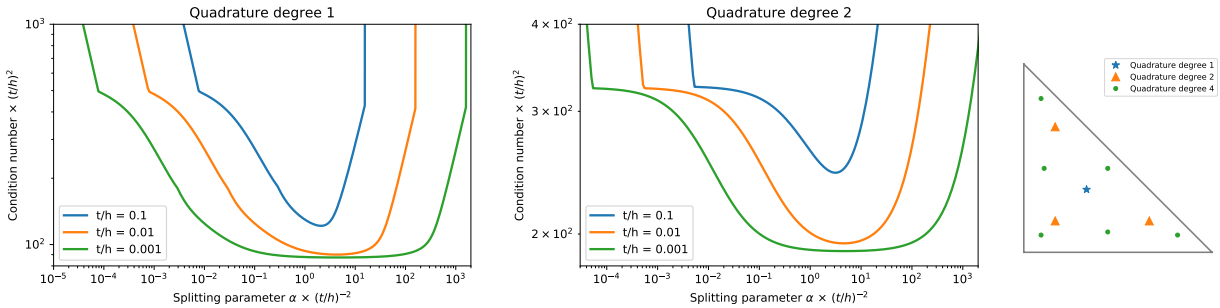

Figure 4: Condition number for a single element non-linear shell element using PSRI discretisation as a function of the splitting ratio α for different thickness t/h. Left: results for a reduced quadrature rule of degree 1; center: quadrature degree 2; right: position of the integration points for the quadrature of orders using the Gauss integration scheme. The results are obtained calculating the eigenvalues of the stiffness matrix a free element linearized around a flat stress-free configuration and eliminating the vanishing eigenvalues associated to the six physical rigid-body modes.

unknowns are projected out at assembly time. PSRI is straightforward to implement in FEniCS using UFL [4].

The numerical experiments of Lovadina and Auricchio [61] for the Reissner-Mindlin problem have shown that an optimal choice of the splitting parameter is $\alpha = t^2/h^2$ for each $T \in \mathcal{T}_h$. In [61], the adopted criterion for this choice was the minimization of the condition number of the stiffness matrix of a single element, calculated after factoring out the zero eigenvalues associated with the physical rigid body modes. We performed a similar analysis for the case non-linear shell PSRI element, linearized around a flat stress-free configuration. Figure 4 reports our results for the single element condition number as a function of the splitting parameter α. In our numerical experiments, we used a Gauss quadrature rule of degree 4 with 6 points of integration on the portions of the energy functional (43) weighted by α. Figure 4-left and Figure 4-center show the condition number obtained for reduced quadrature schemes of order 1 (1 gauss points) and 2 (3 gauss points) on the portion of the energy weighted by $1-\alpha$, respectively. The position of the quadrature points for the different adopted quadrature orders are resumed in Figure 4-right.[2] The two plots confirm that the optimal splitting parameter is of the order of t^2/h^2, independently of the thickness. Moreover, around the optimal point the sensitivity of the condition number with respect to α is weak, a result which is in agreement with our systematic observation of a weak dependence on the convergence rate on the precise value of α, once setting $\alpha \simeq t^2/h^2$. The existence of an optimal value of α is a result of two competing effets: for $\alpha \to 0$ the minimal eigenvalue vanishes, whilst for $\alpha \to 1$ the maximal eigenvalue becomes very large, because of membrane and shear locking. We do not have any analytical proof for the scaling of the optimal splitting parameter, but we observe that the condition $\alpha \simeq t^2/h^2$ seem natural, being the one for which the terms $\alpha\Pi^m$ and $\alpha\Pi^s$ in (43) become of the same order of the bending energy Π^b.

When using a reduced integration rule of degree 1, we observe the appearance of a spurious zero-stiffness mode for $\alpha \simeq t/h$, corresponding to the singularities of the condition number in Figure 4-left. Indeed, we experienced numerical instabilities in several numerical tests when using a

[2]The use of the Gauss quadrature rule and the adopted finite element spaces automatically guarantee what the is referred in the literature as *element isotropy*, *e.g.* the invariance with respect to local nodal numbering.

one-point reduced integration rule. In practice, to avoid the numerical instabilities, we adopted in FEniCS-Shells the reduced quadrature rule of degree 2, that is equally effective in alleviating the locking effect, without introducing any spurious zero-stiffness mode, see Figure 4-center. With this integration scheme the combination of a high-order polynomial space with a PSRI approach for alleviating membrane- and shear-locking seems both simple and effective. The performance of the method being robust with respect to the splitting parameter, once setting $\alpha \simeq t^2/h^2$. The possible instabilities for the one-point quadrature rule are in apparent contrast with the analysis of Arnold and Brezzi [9] and deserve further theoretical and numerical investigations which are out of the scope of the present work.

3.6. Curved Shells

Finally, we describe how the curved shell geometry required for the linear and non-linear Naghdi models is implemented in FEniCS. We use an exact geometry approach, describing the mid-surface of the shell as a closed-form map $\phi_0 : \omega \to \mathbb{R}^3$. For example, for a cylindrical geometry we have $(x_0, x_1) \in \omega := [-\pi/2, \pi/2] \times [0, L]$ and the map $\phi_0 = \{\rho \sin x_0, x_1, \rho \cos x_0\}$. From this, we can calculate approximations of the metric a_0 and curvature b_0 tensors and the normal n_0 of the middle surface from the map ϕ_0 using UFL. Further derived quantities required, e.g. the contravariant components of the metric tensor $a_0^{\alpha\beta}$ and the elasticity tensor $A^{\sigma\beta\sigma\tau}$, can be straightforwardly expressed using UFL. An abbreviated Python code giving an indication for how the curved shell model can be implemented is given in Figure 5, extracted from the documented demo *Clamped semi-cylindrical Naghdi shell under point load* provided in the supplementary material.

4. Examples

To verify the convergence of the adopted discretisation techniques and illustrate the capabilities of the FEniCS-Shells library, we report some benchmark examples. We select eight test cases, including two linear Reissner-Mindlin plates (Section 4.1), two for linear Naghdi shells (Section 4.2), one for Marguerre-von Kármán shallow shells (Section 4.3), and three for nonlinear Naghdi shells (Section 4.4). The linear plate examples are discussed in more detail for testing the performance of our implementation of the MITC formulation; we also showcase here an adaptive remeshing example included in FEniCS-Shells. For linear shells we consider both membrane- and bending-dominated regimes while the non-linear shell examples serve to check them in large displacements and rotation regimes and are based on the FEniCS-Shells PSRI for curing the membrane and bending locking. The example on the thermal buckling of a Marguerre-von Kármán shallow shell of Section 4.3 is proposed here for the first time as a benchmark test of finite element shell models. For all the testing problems we use triangular meshes.

4.1. Reissner-Mindlin plate

In this section we demonstrate the correct convergence rate of our implementation of the Durán–Liberman element for the Reissner-Mindlin plate problem towards a manufactured analytical solution. Then, we show an implementation of a residual-based a posteriori error estimator which we use to drive mesh adaptivity, resolving the solution in a re-entrant plate problem with strong boundary layers.

```
from dolfin import *; from mshr import *; import numpy as np
rho = 1.016; L = 3.048 # radius and length
mesh = generate_mesh(Rectangle(Point(-np.pi/2., 0.), Point(np.pi/2., L)), 21)
# Material properties and thickness
E, nu, t = 2.0685E7, 0.3, 0.03; mu = E/(2.0*(1.0 + nu)); lmbda = 2.0*mu*nu/(1.0 - 2.0*nu)
# Cylindrical map
initial_shape = Expression(('r*sin(x[0])','x[1]','r*cos(x[0])'), r=rho, degree = 4)
V_phi =  FunctionSpace(mesh, VectorElement("Lagrange", triangle, degree = 2, dim = 3))
phi0 = project(initial_shape, V_phi)
# Normal
V_n = FunctionSpace(mesh, VectorElement("Lagrange", triangle, degree = 1, dim = 3))
nv = cross(phi0.dx(0), phi0.dx(1))
n0 = project(nv/sqrt(inner(nv, nv)), V_n) # surface normal in the reference configuration
# Director
director = lambda beta: as_vector([sin(beta[1])*cos(beta[0]), -sin(beta[0]), cos(beta[1])*cos(beta[0])])
beta0_expression = Expression(["atan2(-n[1], sqrt(pow(n[0],2) + pow(n[2],2)))", "atan2(n[0],n[2])"], n = n0, degree=4)
V_beta = FunctionSpace(mesh, VectorElement("Lagrange", triangle, degree = 2, dim = 2))
beta0 = project(beta0_expression, V_beta)
d0 = director(beta0) # director in the reference configuration
# Finite element space
P2, bubble = FiniteElement("Lagrange", triangle, degree = 2), FiniteElement("B", triangle, degree = 3)
enriched = P2 + bubble
U, Beta = VectorElement(enriched, dim=3), VectorElement(P2, dim=2) # element for displacements and rotations
Q = FunctionSpace(mesh, MixedElement([U, Beta])) # Mixed element
# Definitions of functions, test functions, and trial functions
q_ = Function(Q); q, q_t = TrialFunction(Q), TestFunction(Q); u_, beta_ = split(q_)
# Kinematics
F = grad(u_) + grad(phi0) # gradient of the transformation
d = director(beta_+ beta0) # direction
# Initial metric and curvature
a0 = grad(phi0).T*grad(phi0); a0_c = inv(a0); j0 = det(a0)
b0 = -0.5*(grad(phi0).T*grad(d0) + grad(d0).T*grad(phi0))
# Deformations
e = lambda F: 0.5*(F.T*F - a0) # membrane deformation
k = lambda F, d: -0.5*(F.T*grad(d) + grad(d).T*F) - b0 # bending deformation
gamma = lambda F, d: F.T*d-grad(phi0).T*d0 # shear deformation
# Contravariant Hooke's tensor.
i, j, l, m = Index(), Index(), Index(), Index()
A = as_tensor((((2.0*lmbda*mu)/(lmbda + 2.0*mu))*a0_c[i,j]*a0_c[l,m] + mu*(a0_c[i,l]*a0_c[j,m] + a0_c[i,m]*a0_c[j,l])), [i,j,l,m])
# Stress
N = as_tensor(t*A[i,j,l,m]*e(F)[l,m],[i, j]) # membrane stress
M = as_tensor((t**3/12.0)*A[i,j,l,m]*k(F,d)[l,m],[i, j]) # bending moment
T = as_tensor(t*mu*a0_c[i,j]*gamma(F,d)[j], [i]) # shear stress
# Energy densities
psi_m = 0.5*inner(N, e(F)) # membrane energy
psi_b = 0.5*inner(M, k(F,d)) # bending energy
psi_s = 0.5*inner(T, gamma(F,d)) # shear energy
# Total energy functional including PSRI
h = CellDiameter(mesh); alpha = project(t**2/h**2, FunctionSpace(mesh,'DG',0))
dx_h = dx(metadata={'quadrature_degree': 2}) # measure with reduced integration
Pi_PSRI = psi_b*sqrt(j0)*dx + alpha*psi_m*sqrt(j0)*dx + alpha*psi_s*sqrt(j0)*dx
        + (1.0 - alpha)*psi_s*sqrt(j0)*dx_h + (1.0 - alpha)*psi_m*sqrt(j0)*dx_h
# First and second directional derivatives to calculate residual and Hessian
F = derivative(Pi_PSRI, q_, q_t)
J = derivative(F, q_, q)
```

Figure 5: Abbreviated Python code showing construction of energies for half-cylinder non-linear Naghdi model (see Section 4.4). For further details we refer the reader to the documented demo *Clamped semi-cylindrical shell under point load* provided as the supplementary material.

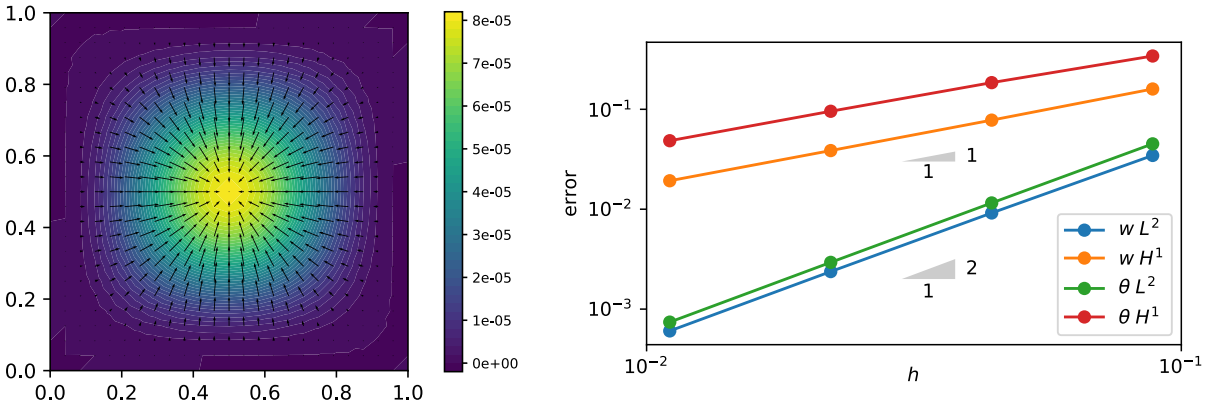

Figure 6: Chinosi clamped plate problem solved using Durán–Liberman element: Transverse displacements (scalar field, density plot) and rotations (vector field, quiver plot, 50% of points discarded) (left). Convergence to Chinosi analytical solution on sequence of uniformly refined meshes in H^1 and L^2 norms for $t = 10^{-4}$ (right).

4.1.1. Clamped square plate

We solve the problem of a unit-square Reissner-Mindlin plate $\Omega = (0, 1)^2$ clamped with uniform thickness $t = \epsilon = 10^{-4}$, and with isotropic linear elastic material behaviour with Youngs modulus $E = 10920$ and Poisson ratio $\nu = 0.3$. The plate is clamped on the boundary (homogeneous Dirichlet boundary conditions on the transverse displacements and rotations) and loaded by a uniform pressure. The closed-form polynomial expressions for the loading and the resulting solution fields are given in Appendix A.

Figure 6 shows the solution to the above problem obtained with FEniCS-Shells using a 32×32 cross-pattern mesh (left) and the error with respect to the analytical solution on a sequence of uniformly refined meshes in both the H^1 and L^2 norms (right). The convergence result given in the original paper of Durán and Liberman [35] is:

$$||\theta - \theta_h||_{H^1(\omega,\mathbb{R}^2)} + ||w - w_h||_{H^1(\omega)} \leq Ch||f||_{L^2(\omega)}, \tag{44}$$

where C is some unknown positive constant independent of the cell size h, corresponding to a linear convergence in the H^1-norm for both the transverse displacements and rotation variables. Although no proof is given in [35] we achieve quadratic convergence for both variables in the L^2 norm, the canonical 'one order higher convergence in L^2' behaviour. Figure 7 shows the convergence in the H^1-norm of the transverse displacement w and the rotations θ for varying thickness t. We see a very slight deterioration of the error for a thick plate, but the rate of convergence is nearly identical for thick through to very thin plates.

In conclusion, this benchmark indicates that the implementation of the Durán-Liberman element in FEniCS-Shells is locking-free and optimally convergent. We remark that a finite element method designed without consideration for locking would not converge at all for this problem. A commented code for this test case is given in the documented demo *Clamped Reissner-Mindlin plate under uniform load* (see supplementary material).

4.1.2. Partly-clamped L-shaped plate

This example shows how sophisticated and efficient adaptive remeshing strategies can be easily implemented using FEniCS-Shells. We consider the a posteriori error estimator proposed in [19],

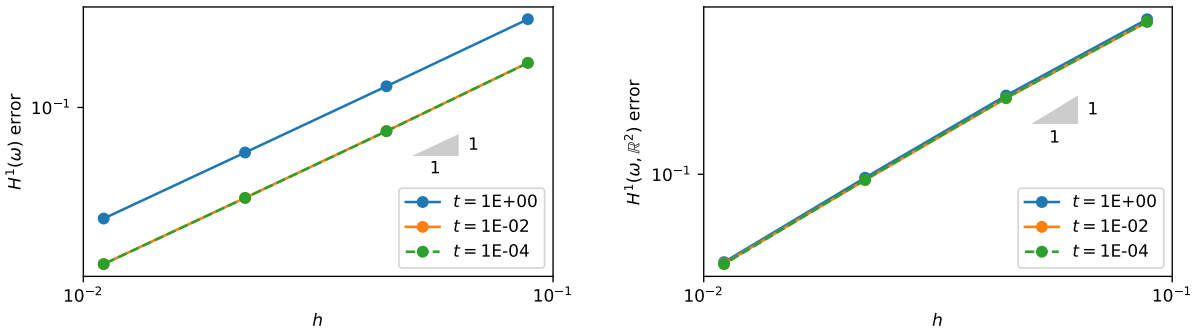

Figure 7: Convergence of Reissner-Mindlin problem discretised with Durán–Liberman element to Chinosi analytical solution for varying thickness parameter t. Left: Error for the transverse displacement w (H^1-norm) as a function of the mesh size h. Right: Error for the rotation field θ (H^1-norm). In the latter case all lines lie on top of each other (convergence behaviour independent of t). We achieve optimal convergence in all cases.

which is similar to the one developed in [27], but it includes extra terms that control the error at boundaries induced by the strong boundary layer present [10] in the Reissner-Mindlin problem as $\epsilon \to 0$. The full specification of the error indicator is given in Appendix B. It is possible to implement these complex expressions in UFL with just a few lines of code and a demo in FEniCS-Shells demonstrates the procedure.

We consider the problem of a non-convex L-shaped plate with a re-entrant corner clamped along the two edges that form the re-entrant corner, and the other four sides left free, Figure 8. The plate is loaded with a uniform transverse load f scaled with the cube of the plate thickness t^3. The material parameters are the same as before. The difficulties of resolving the low regularity solution in the straight corners and in the re-entrant corner, in addition to the strong boundary layers on the free edges, means that a uniform refinement strategy will be very inefficient. Using an a posteriori error estimator to guide the refinement process can lead to orders of magnitude efficiency improvements.

Because no exact analytical solution is known for the studied problem we cannot calculate the exact error. Therefore we resort to comparing the behaviour of the error estimator under both uniform and adaptive refinement strategies.

Figure 9a shows the convergence of the error estimator for a moderately thick plate $t = 10^{-1}$ using adaptive and uniform refinement. The discretisation is based on a Durán–Liberman element. We can see that using uniform refinement we achieve an algebraic convergence rate of only $\mathcal{O}(d^{-1/4})$ where d is the number of degrees of freedom for the discrete system. This corresponds to a classical convergence rate of $\mathcal{O}(h^{1/2})$. This sub-optimal behaviour is expected given the low regularity of the solution particularly in the re-entrant corner. The convergence of the adaptive scheme initially matches that for the uniform refinement before increasing to $\mathcal{O}(d^{-1/2})$ due to the strong local refinements in the re-entrant corner region, and also in the other corners during the latter refinement steps. In Figure 8a we show the meshes at the 2nd and 6th adaptive refinements, with 2,499 and 10,494 degrees of freedom, respectively. The strong refinement near the re-entrant corner is clearly evident.

Critically, we can achieve the same level of convergence with significantly fewer degrees of freedom using the adaptive scheme. Taking the most refined uniformly meshed problem, with 2,365,443 degrees of freedom, we can reach the roughly the same level of error using 123,495 degrees

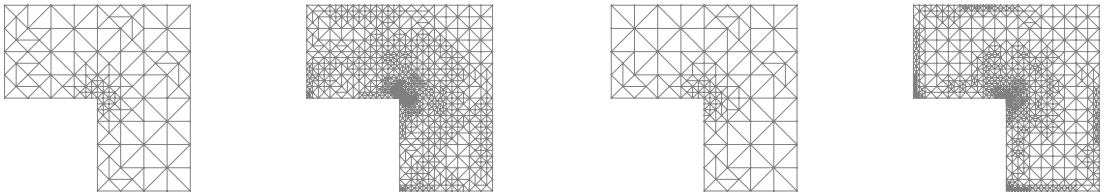

(a) Thick plate ($t = 10^{-1}$) (b) Thin plate ($t = 10^{-4}$)

Figure 8: Meshes after adaptive remeshing at different refinement levels (3rd and 6th level) for thick and thin plates. The increased refinement on the free boundaries for thin plates capture the strong boundary layer effect as $t \to 0$.

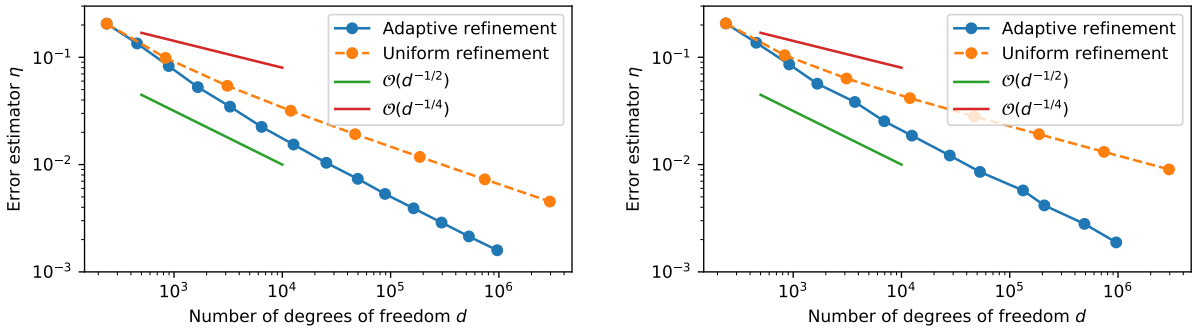

(a) Thick plate ($t = 10^{-1}$) (b) Thin plate ($t = 10^{-4}$)

Figure 9: Plot of error estimator η against the number of cells in the L-shaped plate problem with using adaptive and uniform refinement and Durán–Liberman element. The rate of convergence is significantly improved using the adaptive refinement strategy compared with a uniform refinement strategy.

of freedom with the adaptive strategy.

The trends for a very thin plate with $t = 10^{-4}$ shown in Figure 9b and Figure 8b are broadly similar to those in Figure 8a. However, in addition, because of the presence of the strong boundary layer on the free edges as $t \to 0$, we can see that the error indicator preferentially refines these regions as well as the re-entrant corner.

4.2. Linear Naghdi shell

In this section we demonstrate the performance of the finite element discretisation of the Naghdi linear shell model implemented in the FEniCS-Shells library. The numerical results presented here are based the PSRI formulation. To verify the discretisation in both membrane- and bending dominated regimes two well known benchmark examples have been chosen, namely, a partly clamped hyperbolic paraboloid (bending-dominated test) and an axisymmetric hyperboloid with clamped ends (membrane-dominated test). In both cases, the computational domain is a rectangular domain ω which is mapped to the surface in $\mathbb{R}^3$ through the action of the map ϕ_0.

4.2.1. Partly clamped hyperbolic paraboloid

We consider a thin shell whose middle surface is an hyperbolic paraboloid; the shell is clamped on one of its edges and subject to a uniform load in the vertical direction, see Figure 10 for details.

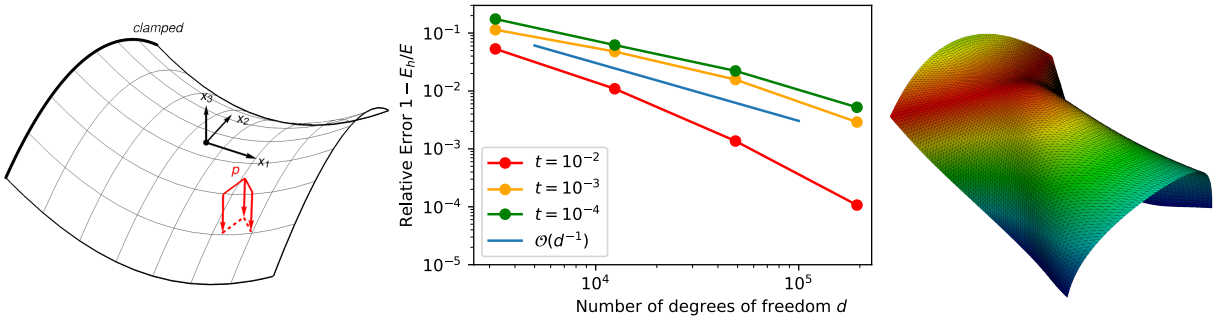

Figure 10: Partly clamped hyperbolic paraboloid with linear Naghdi shell model and PSRI discretisation: initial shape (left), convergence plot (centre), and deformed shape (right). We obtain convergence of $\mathcal{O}(d^{-1})$ in the energy for this problem.

This is an excellent bending dominated benchmark problem to test a FE formulation with respect to membrane-locking issues [17]. The initial shape is the analytical surface $\phi_0 = \{x_0, x_1, x_0^2 - x_1^2\}$ with $(x_0, x_1) \in [-1/2, 1/2] \times [-1/2, 1/2]$. For the simulation we set Poisson ratio to be $\nu = 0.3$. The convergence analysis is performed for thicknesses $t = 10^{-n}$ for $n = 1, 2, 3, 4$ and obtained by setting the uniform pressure load to p to be proportional to t. Convergence rates in strain energy are reported for different values of the dimensionless thinness parameter $t = \epsilon$. The deformed shape of the shell shows two zones corresponding to radically different shell behaviours: a zone where geometry and constraints prevent pure bending displacements (inhibited zone) and a zone where they are allowed (non-inhibited zone). For very thin shells this implies a sharp change of the shell stiffness across the boundary separating the two zones, born out by the bending energy localisation [57].

4.2.2. Axisymmetric hyperboloid with clamped ends

We consider a thin shell whose middle surface is an hyperboloid of revolution; the shell is clamped on both its edges and subjected to a surface axisymmetric normal pressure, so that symmetry arguments enable us to solve the problem over a smaller computational domain (1/8th of the whole domain), see Figure 11 for details. This is a well-posed membrane dominated benchmark problem [44]. The initial shape is the analytical surface $\phi_0 = \{\cos x_0 \cosh x_1, \sin x_0 \cosh x_1, \sinh x_1\}$ with $(x_0, x_1) \in [0, \pi/2] \times [-1, 0]$. For the simulation we set Poisson ratio $\nu = 1/3$ and the pressure load $f = f_0 \cos(2x_0)$. Convergence rates in strain energy are reported for different values of the thinness parameter t. The deformed shape of the shell shows a boundary layer of width $\approx 6\sqrt{t}$ near the clamped edge can be recognised, where the mesh must adequately refined for proper convergence. These results are in agreement to what is reported in the literature [44].

4.3. Marguerre-von Kármán shallow shell

We discuss the performance finite element discretisations of the nonlinear Marguerre-von Kármán shallow shell model (see Section 2.2) implemented in the FEniCS-Shells library. We compare here the results obtained with the MITC and PSRI formulations.

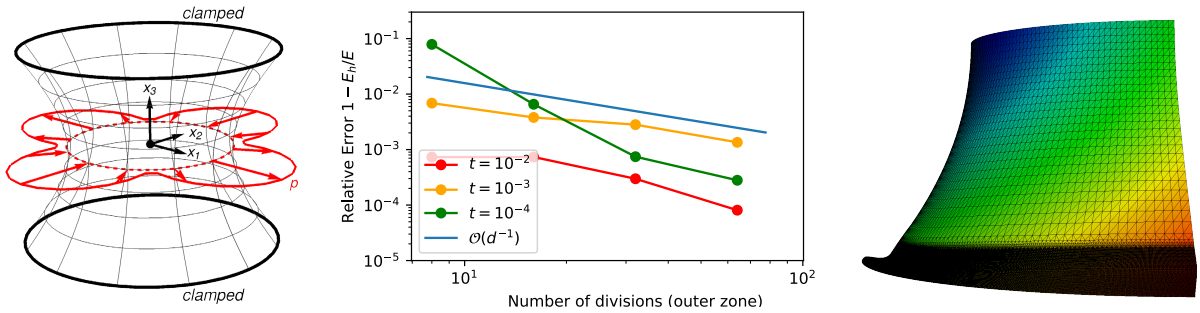

Figure 11: Clamped hyperboloid solved using the PSRI technique: initial shape (left), convergence plot (centre), and deformed shape (right).We obtain convergence of $\mathcal{O}(d^{-1})$ in the energy for this problem. This convergence requires strong refinement in the region of the boundary layer, shown on the deformed shape (right).

4.3.1. Lenticular plate with inelastic curvature

We consider an initially flat isotropic linear elastic disk of radius a with lenticular thickness subject to a through-the-thickness temperature gradient. Thus, the initial shape of the plate is the disk $x_0^2 + x_1^2 \leq a^2$ and the thickness varies as $(1 - x_0^2/a^2 - x_1^2/a^2)\, t$, where t is the maximal thickness at the center. This special shape has been proposed by Mansfield[64, 65] to avoid boundary layer effects and obtain a prestressed plate allowing for an exact analytical solution in the nonlinear regime. The temperature gradient is modelled as a uniform isotropic inelastic curvature $\bar{k}$ with $\bar{k}_{xx} = \bar{k}_{yy} = k_T$ and $\bar{k}_{xy} = 0$ (with $x_0 = x, x_1 = y$). Mansfield has shown that in the framework of the von Kármán model the exact solution of the problem is with uniform curvature in space. The curvature tensor at the equilibrium is with $k_{xy} = 0$ and

$$\begin{cases} \text{for } k_T \leq k_T^*, \quad k_x = k_y : \quad k_x + \dfrac{4}{(1+\nu)^2} \dfrac{k_x^3}{k_T^{*2}} = k_T \\ \\ \text{for } k_T > k_T^*, \quad k_x, k_y = k_T \pm \sqrt{k_T^2 - k_T^{*2}} \end{cases}, \qquad k_T^* = \frac{t}{r^2} \frac{2}{1+\nu} \sqrt{\frac{2(7+\nu)}{(1+\nu)}}. \tag{45}$$

For $k_T \ll k_T^*$, the behaviour is approximately linear. The equilibrium curvature k is spherical and close to $\bar{k}$. However, conforming the plate to a spherical surface implies membrane extension. For $k_T \gg k_T^*$, the extensional deformation becomes too expensive from the energetic point of view and the minimal energy configurations are approximately cylindrical and bending-dominated. The critical value k_T^* corresponds to a bifurcation from the spherical shape. For $k \simeq k_T^*$ bending and extensional energies are of the same order. In the perfectly isotropic case, for $k > k_T^*$ the plate is neutrally stable: all the shapes obtained by rotating the curvature axis are still solutions of the problem. This structure was a source of inspiration for several recent works on morphing plates and shells[89, 90, 43].

We perform simulations increasing the inelastic curvature k_T, for a Poisson ration $\nu = 0.3$ and maximum thickness $t = 0.01$. The Young modulus has no influence here. To break the rotational symmetry, we introduce a slight imperfection in the inelastic curvature imposing $\bar{k}_x = k_T/\rho$, $\bar{k}_y = k_T\rho$ with $\rho = 0.998$. Figure 12 shows the bifurcation diagrams obtained with the MITC and the PSRI discretisations for the shearable version of the model exposed in Section 2.2. We use uniform unstructured triangular meshes and parametrise the mesh size by the number of division n along the radius. To avoid rigid body motions, we applied suitable pointwise Dirichlet boundary conditions. Namely we set to zero all the components of the displacement at the

center, the displacement in x direction at $(0, a)$ and the displacement in y direction at $(a, 0)$. The analytical solution (45) is reported in the plot as solid blue line. The results obtained with both the discretisations converge to the analytical solution. However, PSRI converges more quickly than MITC, giving very good results even with $n = 5$. A possible explanation is that membrane locking is not cured in our MITC implementation. Further developments should attempt to implement in FEniCS-Shells more advanced MITC techniques that are known to better perform with respect to membrane locking [53, 29, 46, 16]. However, we conclude that the PSRI technique introduced in FEniCS-Shells is a very efficient discretisation to cure both shear and membrane locking in the weakly nonlinear regime. This will be further tested and assessed in the next Section. To introduce fully nonlinear models, we compare in Figure 13 the results obtained with the fully nonlinear Naghdi shell model and the Marguerre-von Kármán shallow shell model. In both cases we use the PSRI discretisation. As expected [58], the results confirm that Marguerre-von Kármán model can safely be used to approximate the Naghdi model for sufficiently small loadings, namely for curvatures of the order of a^2/t. More surprisingly, for the present test the discrepancies with respect the fully nonlinear model remain tolerable also for $k \simeq 50\, a^2/t$. The documented demo *Buckling of a heated von Kármán plate* in the supplementary material includes the full commented code for the Marguerre-von Kármán shallow shell with PRSI discretisation. An extension of this problem to the case of an orthotropic material is included in FEniCS-Shells as a further documented demo in order to illustrate some basic tools for modelling composite laminates that we do not explicitly describe in this paper.

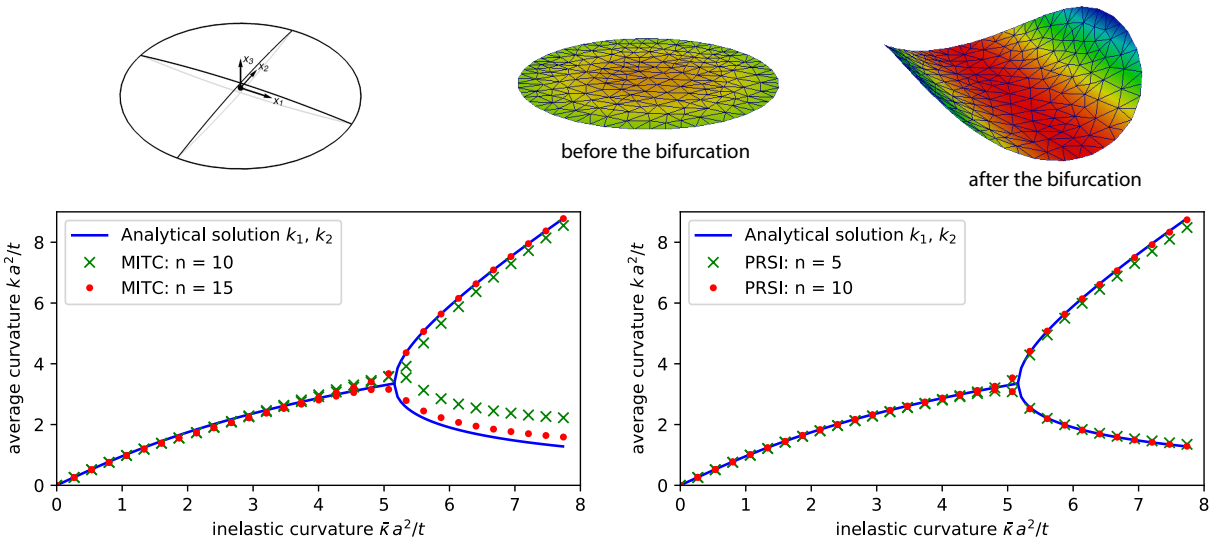

Figure 12: Lenticular orthotropic plate. Bottom row: Bifurcation diagram for the curvatures k_x and k_y at the equilibrium as a function of the temperature loading. The curvature values reported in the plots as dots are the spatial average extracted from the finite element results with the MITC (left) and PRSI (right) models with uniform unstructured meshes with $n \in [5, 10]$ divisions along the radius. The top row: Sketch of the lenticular plate (left) and snapshots of the equilibrium shapes before (center) and after (right) the bifurcation. The results are for $a^2/t = 100$ and $\nu = 0.3$.

4.4. Nonlinear Naghdi shell

We demonstrate here the performance of the finite element discretisation of the nonlinear Naghdi shell model implemented in the FEniCS-Shells library. To test the predictive capability of the

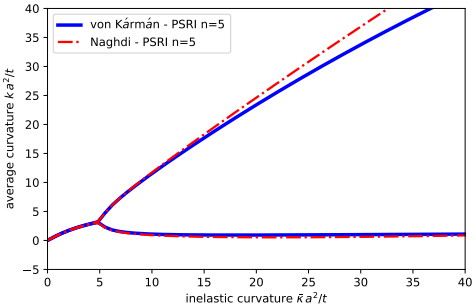

Figure 13: Lenticular orthotropic plate. Comparison of the results obtained with the von Kármán and the Naghdi models using the PSRI discretisation and an unstructured uniform mesh with $n = 5$ division along the radius. The results are for $a^2/t = 100$ and $\nu = 0.3$.

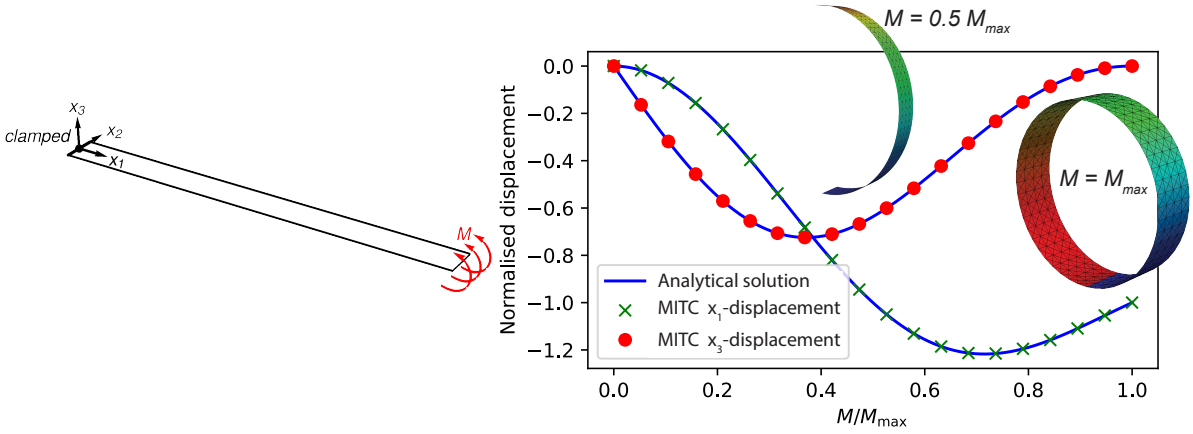

Figure 14: Cantilever plate under end moment. Left: initial geometry and loading. Right: Comparison between analytical and numerical solution (MITC) for the moment-displacement diagram, where the insets show the deformed configurations for $M = 0.5M_{\max}$ and $M = M_{\max}$. We report here the results for displacement at the free end in the X_1 and X_3 directions, normalised with the initial length L.

formulation in the large displacements and rotations regime we selected three well known benchmark problems, see [47] and references therein.

4.4.1. Cantilever plate under end moment

We consider a strip clamped on one of its edges and subjected to a moment M on the other edge, see Figure 14 for details. In its natural configuration the shell occupies a flat rectangular domain of width b, length L. In the numerical simulations we set $L = 12b$, thickness $t = b/10$, and Poisson ratio $\nu = 0$. For load $M = 2\pi EI/L$, where $I = t^3/12$ the plate completely rolls up on itself. The normalised vertical and horizontal displacements at the free end have the analytical expressions $w/L = (1 - \cos 2\pi\mu)/(2\pi\mu)$ and $v/L = \sin(2\pi\mu)/(2\pi\mu) - 1$, respectively, where $\mu = M/M_{\max}$. A comparison between the finite element and analytical solutions in terms of load-deflection curves is reported in Figure 14. The numerical solution is computed by discretising the domain with a 48×4 element mesh and shows excellent agreement with the analytical one. The insets show the deformed configurations of the plate for two values of the end moment.

4.4.2. Slit annular plate under end shear force

We consider a slit annular plate of internal radius $R_1 = 6$ and external radius $R_2 = 10$ clamped on one of its edges and subjected to a line shear load p on the other edge, see Figure 15 for details. A comparison between the finite element and reference solutions in terms of load-deflection curves is

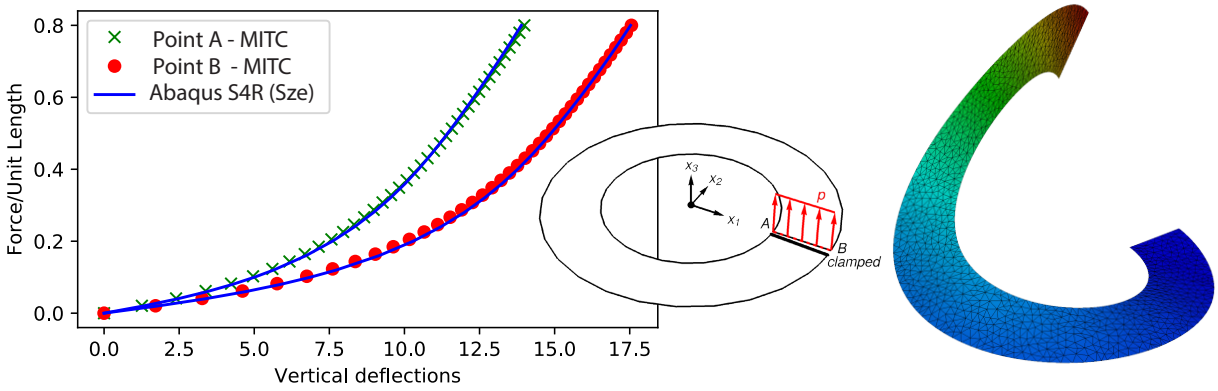

Figure 15: Slit annular plate subjected to a line vertical load. The load-deflection diagram compare the numerical solution obtained with FEniCS-Shells MITC discretisation with a reference solution (Sze [92], Abaqus S4R). Right: geometry and loading; Left: final deformed configuration. Excellent agreement between the result of Sze [92] and FEniCS-Shells is achieved.

reported in Figure 15, where we set the thickness $t = 0.03$, Poisson ratio $\nu = 0$ and maximum load $p = 0.8E$, with $E = 21 \times 10^6$. The numerical solution is computed by discretising the domain with a 28−division unstructured mesh and the MITC technique. The reference solution [92] is computed on a 10×80 Abaqus S4R-element mesh. We see excellent agreement between the two results.

4.4.3. Clamped semi-cylindrical shell under point load

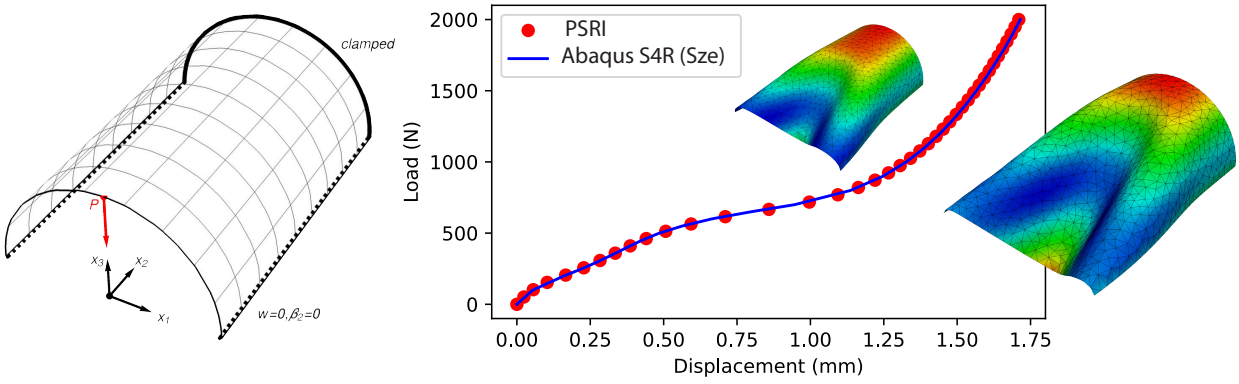

Figure 16: Clamped semi-cylindrical shell under point load. Left: Initial configuration and boundary conditions. Right: Comparison of the results of the PSRI implementation with a reference solution (Sze [92], Abaqus S4R). The insets show the deformed configurations for $P = P_{max}$ and $P = P_{max}/2$. Notice the stiffening of the shell beyond a load of around 750N.

We consider a semi-cylindrical shell clamped on one of its curved edges and subjected to a point load P at the centre of the free curved edge. Along its straight longitudinal edges the transverse displacement and the normal rotation are restrained, see Figure 16 for details.

The computational domain is a rectangle $(x_0, x_1) \in [-\pi/2, \pi/2] \times [0, 3.048]$ which is mapped to the natural configuration semi-cylindrical shell of radius $\rho = 1.016$ through the initial transformation $\phi_0(x_0, x_1) = \{\rho \sin x_0, x_1, \rho \cos x_0\}$. A comparison between the FE and reference solution in terms of load-deflection curves is reported in Figure 16 for the thickness $t = 0.03$, Young modulus $E = 2.0685 \times 10^7$, Poisson ratio $\nu = 0.3$, and a maximum load $P_{\max} = 2000$. The numerical solution is computed by discretising the domain with a $21-$division unstructured mesh and shows a very good agreement with the reference solution in [92] computed on a 40×40 ABAQUS S4R-element mesh. For a complete commented code for this test case we refer to the documented demo *Clamped semi-cylindrical Naghdi shell under point load*, available in the supplementary material.

5. Conclusions

In this paper we shown how a high-level approach to specifying thin structural models, in conjunction with automatic code generation tools, can lead to simple, extensible and effective finite element plate and shell formulations. The power of this approach is demonstrated via the open-source FEniCS-Shells library. We have shown the main mathematical aspects of the structural models available and the numerical procedures used to discretise them, with a particular emphasis on shear- and membrane-locking issues.

We selected two main discretisation strategies: a special implementation of the MITC technique that provides an effective cure for shear-locking in linear plate models, and an extension to nonlinear shells of the PRSI strategy proposed in [9] for nonlinear shell problems shear- and membrane-locking. The examples section, accompanied by a set of documented demos, while by no means exhaustive, shows the capabilities of the proposed methods and the type of analyses that can be performed. Each discretisation strategy has its advantages and drawbacks. On one hand, the PSRI is simple and effective for linear and nonlinear problem, but it requires the setting of an artificial splitting parameter. Even if we provided specific guidances for its choice and the numerical tests show a very low sensitivities of the accuracy of the results on its precise value (see Figure 4), this remains an undesired aspect. On the other hand, our MITC technique is specifically designed for shear locking, but is less effective for membrane locking, as shown by the example in Figure 12. A natural extension of the present work should consider other types of MITC elements with higher-order interpolations and/or improved tying rules and geometries which are known to better perform with respect to membrane locking [see *e.g.* 46, 53, 18]. Developing automated tools to perform classical tests such as the patch test or the test of the inf-sup stability conditions, would be a further appropriate extension that could meet the expectations of the community working on finite element engineering.

We believe that FEniCS-Shells will be a helpful contribution for researchers and graduate students in the community simulating thin structures. FEniCS-Shells could provide users with efficient and simple tools to implement specific solvers for multilayered or other specific plate and shell models [85], shell models including multiphysical couplings or nonlinear material behaviour [84, 52, 43], as well as one atom thick shell structures such as nanotubes and graphene [11]. Because of its flexibility and the easiness in the development of user models and fine control of the different aspects of the solution process, it can conveniently complement the offer of commercial finite element packages and other open-source projects.

The present work constitutes an instrumental step in a larger project on the mechanics and physics of shell structures, including the analysis of the nonlinear material behaviour and fracture of isotropic and anisotropic shells [6, 8, 7] through phase-field variational models [25, 45, 68], applications to multistable structures with embedded active materials [43, 88], and for the understanding of singularities and energy scalings in plates and shells [33]. Current and future technical developments of FEniCS-Shells will be aimed at providing anisotropic adaptive remeshing tools [87, 69] and coupling to advanced nonlinear solvers, such as asymptotic numerical continuation methods [93] and deflation techniques [36] to automatically detect multiple solutions of nonlinear systems. A further interesting extension would be to adapt to shell modelling the special approach proposed by [83] for solving PDEs on manifolds with FEniCS.

Appendix A. Closed-form solution for a Reissner-Mindlin clamped square plate with polynomial loading

This analytical solution is taken from the paper [30]. With transverse loading:

$$f(x,y)/D = 12y(y-1)(5x^2-5x+1)\left\{2y^2(y-1)^2+x(x-1)(5y^2-5y+1)\right\} + 12x(x-1)(5y^2-y+1)\left\{2x^2(x-1)^2+y(y-1)(5x^2-5x+1)\right\}, \quad \text{(A.1)}$$

with $D = Et^3/[12(1-\nu^2)]$, it is possible to obtain the following closed-form solutions for the rotations and transverse displacements:

$$\theta(x,y) = \left\{y^3(y-1)^3x^2(x-1)^2(2x-1),\ x^3-1)y^2(y-1)^2(2y-1)\right\}^T \quad \text{(A.2a)}$$

$$w(x,y) = \frac{1}{3}x^2(x-1)^3(y-1)^3 - \frac{2t^2}{5(1-\nu)}[y^3(y-1)^3x(x-1)(5x^2-5x+1) \quad \text{(A.2b)}$$

$$+\ x^3(x-1)^3y(y-1)(5y^2-5y+1)]. \quad \text{(A.2c)}$$

Appendix B. Residual-based a posteriori error estimator

The key result found in the paper[19] is that the error between the finite element solution and the exact solution defined in the following sense:

$$|||(\theta-\theta_h, w-w_h)|||_h + t||\gamma-\gamma_h||_{L^2(\Omega)} + ||\gamma-\gamma_h||_{H^{-1}(\Omega)} + t^2||\operatorname{rot}(\gamma-\gamma_h)||_{L^2(\Omega)}, \quad \text{(B.1)}$$

where the mesh-dependant norm $|||(\theta,w)|||_h$ is defined by:

$$|||(\theta,w)|||_h^2 = ||\theta||_{H^1(\Omega)}^2 + \sum_{T\in\mathcal{T}_h}\frac{1}{t^2+h_T^2}||\nabla w-\theta||_{L^2(T)}^2, \quad \text{(B.2)}$$

can be controlled by an error estimator of the following form:

$$\eta_h^2 = \sum_{T\in\mathcal{T}_h}(\eta^2+\rho^2) + \sum_{E\in\mathcal{E}_h^{\text{int}}}\eta_{\text{int}}^2 + \sum_{E\in\mathcal{E}_h^{\text{free}}}\eta_{\text{free}}^2, \quad \text{(B.3a)}$$

$$\eta^2 = h_T^2(h_T^2+t^2)||f+\operatorname{div}\gamma_h||_{L^2(T)}^2 + h_T^2||\operatorname{div}M_h+\gamma_h||_{L^2(T)}^2, \quad \text{(B.3b)}$$

$$\eta_{\text{int}}^2 = h_E(h_E^2+t^2)||[\![\gamma_h\cdot n]\!]||_{L^2(E)} + h_E||[\![M_h n]\!]||_{L^2(E)}^2, \quad \text{(B.3c)}$$

$$\eta_{\text{free}}^2 = h_E||M_h n||_{L^2(E)}^2 + h_E(h_E^2+t^2)||\gamma_h\cdot n||_{L^2(E)}^2, \quad \text{(B.3d)}$$

$$\rho^2 = ||\operatorname{rot}(I-R_h)\theta_h||_{L^2(T)}^2 + ||(I-R_h)\theta_h||_{L^2(T)}^2, \quad \text{(B.3e)}$$

where $\mathcal{E}_h^{\text{free}} \not\subset \mathcal{E}_h^{\text{int}}$ are the subset of edges on the free boundary (natural boundary conditions).

Acknowledgements

We would like to thank Douglas N. Arnold for sharing his implementation of the unreduced Durán-Liberman element in the Unified Form Language with us. We also sincerely thank Patrick Farrell and Garth Wells for giving us their feedback on a preliminary version of this manuscript.

Jack S. Hale is supported by the National Research Fund, Luxembourg, and cofunded under the Marie Curie Actions of the European Commission (FP7-COFUND) Grant No. 6693582.

Stéphane P. A. Bordas thanks partial funding for his time provided by the European Research Council Starting Independent Research Grant (ERC StG) Grant No. 279578 entitled "Towards real time multiscale simulation of cutting in non-linear materials with applications to surgical simulation and computer guided surgery".

Matteo Brunetti and Corrado Maurini acknowledge the financial support of Project ANR-13-JS09-0009 (Agence Nationale de la Recherche, 2014).

Supporting information

Code (LGPLv3), documentation and demos are available from the links at: https://doi.org/10.6084/m9.figshare.4291160.

Three documented demos are formally enclosed as supplementary materials:

(S1) `Clamped-Reissner-Mindlin-plate-under-uniform-load.pdf`

(S2) `Buckling-heated-von-Karman-plate.pdf`

(S3) `Clamped-semi-cylindrical-w-shell-under-point-load.pdf`

References

[1] Mat-fem: Learning the finite element method with matlab and gid, 2012. URL http://www.cimne.com/mat-fem.

[2] *ABAQUS Theory Guide, Version 2017*. Simulia, 2016.

[3] M. Ainsworth and K. Pinchedez. The hp-MITC finite element method for the Reissner-Mindlin plate problem. *Journal of Computational and Applied Mathematics*, 148(2):429–462, November 2002. ISSN 0377-0427. doi: 10.1016/S0377-0427(02)00560-5. URL http://www.sciencedirect.com/science/article/B6TYH-472HT8V-9/2/006aa5725265e03487fd00f261e18249.

[4] M. Alnæs, J. Blechta, J. Hake, A. Johansson, B. Kehlet, Anders Logg, Chris Richardson, Johannes Ring, Marie E. Rognes, and Garth N. Wells. The FEniCS Project Version 1.5. *Archive of Numerical Software*, 3(100), December 2015. ISSN 2197-8263. doi: 10.11588/ans.2015.100.20553. URL http://journals.ub.uni-heidelberg.de/index.php/ans/article/view/20553.

[5] M. S. Alnæs, A. Logg, K. B. Ølgaard, M. E. Rognes, and G. N. Wells. Unified Form Language: A Domain-specific Language for Weak Formulations of Partial Differential Equations. *ACM Trans. Math. Softw.*, 40(2):9:1–9:37, March 2014. ISSN 0098-3500. doi: 10.1145/2566630. URL http://doi.acm.org/10.1145/2566630.

[6] F. Amiri, D. Millán, Y. Shen, T. Rabczuk, and M. Arroyo. Phase-field modeling of fracture in linear thin shells. *Theoretical and Applied Fracture Mechanics*, 69:102–109, February 2014. ISSN 0167-8442. doi: 10.1016/j.tafmec.2013.12.002. URL http://www.sciencedirect.com/science/article/pii/S0167844213000815.

[7] P. Areias and T. Rabczuk. Finite strain fracture of plates and shells with configurational forces and edge rotations. *International Journal for Numerical Methods in Engineering*, 94(12):1099–1122. doi: 10.1002/nme.4477. URL https://onlinelibrary.wiley.com/doi/abs/10.1002/nme.4477.

[8] P. Areias, T. Rabczuk, and M.A. Msekh. Phase-field analysis of finite-strain plates and shells including element subdivision. *Computer Methods in Applied Mechanics and Engineering*, 312:322 – 350, 2016. ISSN 0045-7825. doi: https://doi.org/10.1016/j.cma.2016.01.020. URL http://www.sciencedirect.com/science/article/pii/S0045782516300196. Phase Field Approaches to Fracture.

[9] D. Arnold and F. Brezzi. Locking-free finite element methods for shells. *Mathematics of Computation of the American Mathematical Society*, 66(217):1–14, 1997. ISSN 0025-5718, 1088-6842. doi: 10.1090/S0025-5718-97-00785-0. URL http://www.ams.org/mcom/1997-66-217/S0025-5718-97-00785-0/.

[10] D. N Arnold and R. S Falk. Asymptotic analysis of the boundary layer for the Reissner-Mindlin plate model. *SIAM Journal on Mathematical Analysis*, 27(2):486–514, 1996.

[11] M. Arroyo and T. Belytschko. Finite crystal elasticity of carbon nanotubes based on the exponential Cauchy-Born rule. *Physical Review B*, 69(11):115415, March 2004. doi: 10.1103/PhysRevB.69.115415. URL https://link.aps.org/doi/10.1103/PhysRevB.69.115415.

[12] B. Audoly and Y. Pomeau. *Elasticity and Geometry. From hair curls to the non-linear response of shells*. Oxford University Press, 2010.

[13] S. Balay, S. Abhyankar, M. F. Adams, Jed Brown, Peter Brune, Kris Buschelman, Lisandro Dalcin, Victor Eijkhout, William D. Gropp, Dinesh Kaushik, Matthew G. Knepley, Lois Curfman McInnes, Karl Rupp, Barry F. Smith, Stefano Zampini, Hong Zhang, and Hong Zhang. PETSc Users Manual. Technical Report ANL-95/11 - Revision 3.7, Argonne National Laboratory, 2016. URL http://www.mcs.anl.gov/petsc.

[14] K. J. Bathe. *Finite Element Procedures*. 2 edition, 2014. ISBN 978-0979004957.

[15] K. J Bathe and E. N Dvorkin. A four-node plate bending element based on Mindlin/Reissner plate theory and a mixed interpolation. *International Journal for Numerical Methods in Engineering*, 21(2):367–383, 1985.

[16] K-J. Bathe, F. Brezzi, and S. W. Cho. The MITC7 and MITC9 Plate bending elements. *Computers & Structures*, 32(3-4):797–814, 1989. ISSN 0045-7949. doi: 10.1016/0045-7949(89)90365-9. URL http://www.sciencedirect.com/science/article/B6V28-47XC0M5-GM/2/f5312a3ba4d9279fb60c8ed5bca5d954.

[17] K-J. Bathe, A. Iosilevich, and D. Chapelle. An evaluation of the mitc shell elements. *Computers & Structures*, 75(1):1–30, 2000.

[18] Klaus-Jürgen Bathe, Alexander Iosilevich, and Dominique Chapelle. An evaluation of the mitc shell elements. *Computers & Structures*, 75(1):1–30, 2000.

[19] L. Beirão da Veiga, C. Chinosi, C. Lovadina, and R. Stenberg. A-priori and a-posteriori error analysis for a family of Reissner–Mindlin plate elements. *BIT Numerical Mathematics*, 48(2):189–213, June 2008. ISSN 0006-3835, 1572-9125. doi: 10.1007/s10543-008-0175-y. URL http://link.springer.com/10.1007/s10543-008-0175-y.

[20] D.J. Benson, Y. Bazilevs, M.C. Hsu, and T.J.R. Hughes. Isogeometric shell analysis: The Reissner-Mindlin shell. *Computer Methods in Applied Mechanics and Engineering*, 199(5-8):276–289, January 2010. ISSN 0045-7825. doi: 10.1016/j.cma.2009.05.011. URL http://www.sciencedirect.com/science/article/B6V29-4WC1126-1/2/b073c14a2534022b5eda8399974d6164.

[21] P. Betsch, A. Menzel, and E. Stein. On the parametrization of finite rotations in computational mechanics: A classification of concepts with application to smooth shells. *Computer Methods in Applied Mechanics and Engineering*, 155(3):273 – 305, 1998. ISSN 0045-7825. doi: https://doi.org/10.1016/S0045-7825(97)00158-8. URL http://www.sciencedirect.com/science/article/pii/S0045782597001588.

[22] M. Bischoff and E. Ramm. Shear deformable shell elements for large strains and rotations. *International Journal for Numerical Methods in Engineering*, 40(23):4427–4449, December 1997. ISSN 1097-0207. doi: 10.1002/(SICI)1097-0207(19971215)40:23⟨4427::AID-NME268⟩3.0.CO;2-9. URL http://onlinelibrary.wiley.com/doi/10.1002/(SICI)1097-0207(19971215)40:23<4427::AID-NME268>3.0.CO;2-9/abstract.

[23] K-U. Bletzinger, M. Bischoff, and E. Ramm. A unified approach for shear-locking-free triangular and rectangular shell finite elements. *Computers & Structures*, 75(3):321–334, April 2000. ISSN 0045-7949. doi: 16/S0045-7949(99)00140-6. URL http://www.sciencedirect.com/science/article/pii/S0045794999001406.

[24] D. Boffi and C. Lovadina. Analysis of new augmented Lagrangian formulations for mixed finite element schemes. *Numerische Mathematik*, 75(4):405–419, 1997.

[25] B. Bourdin, G. A. Francfort, and J. Marigo. The variational approach to fracture. *Journal of Elasticity*, 91(1):5–148, 2008.

[26] F. Brezzi, J. Douglas, and L. D. Marini. Two families of mixed finite elements for second order elliptic problems. *Numerische Mathematik*, 47(2):217–235, June 1985. ISSN 0029-599X, 0945-3245. doi: 10.1007/BF01389710. URL https://link.springer.com/article/10.1007/BF01389710.

[27] C. Carstensen and J. Hu. A Posteriori Error Analysis for Conforming Mitc Elements for Reissner-Mindlin Plates. *Mathematics of Computation*, 77(262):611–632, 2008. ISSN 0025-5718. URL http://www.jstor.org/stable/40234526.

[28] D. Chapelle and K-J. Bathe. *The Finite Element Analysis of Shells - Fundamentals*. Springer, 2nd edition. edition, December 2010. ISBN 3-642-16407-2.

[29] D. Chapelle, D. L. Oliveira, and M. L. Bucalem. MITC elements for a classical shell model. *Computers & Structures*, 81(8-11):523–533, May 2003. ISSN 0045-7949. doi: 10.1016/S0045-7949(02)00408-X. URL http://www.sciencedirect.com/science/article/B6V28-47RJG6P-8/2/7efbc5c5c10fd7ec5a3bf2eb8b557489.

[30] C. Chinosi and C. Lovadina. Numerical analysis of some mixed finite element methods for Reissner-Mindlin plates. *Computational Mechanics*, 16:36–44, April 1995. ISSN 0178-7675, 1432-0924. doi: 10.1007/s004660050046. URL http://www.springerlink.com/content/2v8n92dg407waue3/.

[31] P. G. Ciarlet. *Theory of Shells*. Elsevier, May 2000. ISBN 978-0-08-051123-8. Google-Books-ID: EYAxQ77o_6QC.

[32] F. Cirak, M. Ortiz, and P. Schröder. Subdivision surfaces: a new paradigm for thin-shell finite-element analysis. *International Journal for Numerical Methods in Engineering*, 47(12):2039–2072, 2000. ISSN 1097-0207. doi: 10.1002/(SICI)1097-0207(20000430)47:12⟨2039::AID-NME872⟩3.0.CO;2-1. URL http://dx.doi.org/10.1002/(SICI)1097-0207(20000430)47:12<2039::AID-NME872>3.0.CO;2-1.

[33] S. Conti and F. Maggi. Confining thin elastic sheets and folding paper. *Archive for Rational Mechanics and Analysis*, 187(1):1–48, 2008.

[34] Electricité de France. Finite element *code_aster*, analysis of structures and thermomechanics for studies and research. Open source on www.code-aster.org, 1989–2017.

[35] R. Durán and E. Liberman. On mixed finite element methods for the Reissner-Mindlin plate model. *Mathematics of Computation*, 58(198):561–573, 1992. ISSN 0025-5718, 1088-6842. doi: 10.1090/S0025-5718-1992-1106965-0. URL http://www.ams.org/mcom/1992-58-198/S0025-5718-1992-1106965-0/.

[36] P. E. Farrell, Á. Birkisson, and S. W. Funke. Deflation techniques for finding distinct solutions of nonlinear partial differential equations. *SIAM Journal on Scientific Computing*, 37:A2026–A2045, 2015. doi: 10.1137/140984798.

[37] A. Foppl. *Vorlesungen uber technische Mechanik*. 1907.

[38] G. Gaël, J. Benoît, et al. Eigen v3. http://eigen.tuxfamily.org, 2010.

[39] J. S. Hale, M. Brunetti, S. Bordas, and C. Maurini. FEniCS-Shells. 2016. doi: 10.6084/m9.figshare.4291160.v1. URL https://figshare.com/articles/FEniCS-Shells/4291160.

[40] J. S. Hale, L. Li, C. N. Richardson, and G. N. Wells. Containers for Portable, Productive, and Performant Scientific Computing. *Computing in Science & Engineering*, 19(6):40–50, November 2017. ISSN 1521-9615. doi: 10.1109/MCSE.2017.2421459. URL http://ieeexplore.ieee.org/document/7933304/.

[41] J.S. Hale. *Meshless methods for shear-deformable beams and plates based on mixed weak forms*. PhD thesis, Imperial College London, April 2013. URL http://spiral.imperial.ac.uk/handle/10044/1/14379.

[42] J.S. Hale and P.M. Baiz. A locking-free meshfree method for the simulation of shear-deformable plates based on a mixed variational formulation. *Computer Methods in Applied Mechanics and Engineering*, 241–244(0): 311–322, October 2012. ISSN 0045-7825. doi: 10.1016/j.cma.2012.06.010. URL http://www.sciencedirect.com/science/article/pii/S0045782512001983.

[43] W. Hamouche, C. Maurini, S. Vidoli, and A. Vincenti. Multi-parameter actuation of a neutrally stable shell: a flexible gear-less motor. *Proceedings of the Royal Society of London A: Mathematical, Physical and Engineering Sciences*, 473(2204), 2017. ISSN 1364-5021. doi: 10.1098/rspa.2017.0364. URL http://rspa.royalsocietypublishing.org/content/473/2204/20170364.

[44] J-F. Hiller and K-J. Bathe. Measuring convergence of mixed finite element discretizations: an application to shell structures. *Computers & Structures*, 81(8):639–654, 2003.

[45] A. Ibarra, B. Roman, and F. Melo. The tearing path in a thin anisotropic sheet from two pulling points: Wulff's view. *Soft Matter*, 12(27):5979–5985, 2016.

[46] H-M. Jeon, Y. Lee, P-S. Lee, and K-J. Bathe. The mitc3+ shell element in geometric nonlinear analysis. *Computers & Structures*, 146:91–104, 2015.

[47] H-M. Jeon, Y. Lee, P-S. Lee, and K-J. Bathe. The MITC3+ shell element in geometric nonlinear analysis. *Computers & Structures*, 146:91–104, January 2015. ISSN 0045-7949. doi: 10.1016/j.compstruc.2014.09.004. URL http://www.sciencedirect.com/science/article/pii/S0045794914001977.

[48] P. Kere and M. Lyly. Reissner–mindlin–von kármán type plate model for nonlinear analysis of laminated composite structures. *Composite structures*, 71(3):289–292, 2005.

[49] J. Kiendl, K.-U. Bletzinger, J. Linhard, and R. Wüchner. Isogeometric shell analysis with Kirchhoff–Love elements. *Computer Methods in Applied Mechanics and Engineering*, 198(49-52):3902–3914, November 2009. ISSN 00457825. doi: 10.1016/j.cma.2009.08.013. URL http://linkinghub.elsevier.com/retrieve/pii/S0045782509002680.

[50] R. C. Kirby and A. Logg. A Compiler for Variational Forms. *ACM Trans. Math. Softw.*, 32(3):417–444, September 2006. ISSN 0098-3500. doi: 10.1145/1163641.1163644. URL http://doi.acm.org/10.1145/1163641.1163644.

[51] G. R. Kirchhoff. Uber das gleichgewicht und die bewegung einer elastischen scheibe. 1850.

[52] Y. Klein, E. Efrati, and E. Sharon. Shaping of elastic sheets by prescription of non-Euclidean metrics. *Science*, 315:1116–1120, February 2007.

[53] Yeongbin Ko, Phill-Seung Lee, and Klaus-Jürgen Bathe. A new mitc4+ shell element. *Computers & Structures*, 182:404 – 418, 2017. ISSN 0045-7949. doi: https://doi.org/10.1016/j.compstruc.2016.11.004. URL http://www.sciencedirect.com/science/article/pii/S0045794916309464.

[54] W. T. Koiter. A consistent first approximation in the general theory of thin elastic shells. *The theory of thin elastic shells*, pages 12–33, 1959.

[55] Warner T Koiter. On the foundations of linear theory of thin elastic shells. 1. *Proceedings of the Koninklijke Nederlandse Akademie van Wetenschappen Series B-Physical Sciences*, 73(3):169, 1970.

[56] J. Korelc. Multi-language and Multi-environment Generation of Nonlinear Finite Element Codes. *Engineering with Computers*, 18(4):312–327, November 2002. ISSN 0177-0667, 1435-5663. doi: 10.1007/s003660200028. URL https://link.springer.com/article/10.1007/s003660200028.

[57] P-S. Lee and K-J. Bathe. On the asymptotic behavior of shell structures and the evaluation in finite element solutions. *Computers & structures*, 80(3):235–255, 2002.

[58] M. Lewicka, L. Mahadevan, and M.R. Pakzad. Models for elastic shells with incompatible strains. *Proceedings of the Royal Society A: Mathematical, Physical and Engineering Sciences*, 470(2165):20130604–20130604, February 2014.

[59] A. Logg and G. N. Wells. DOLFIN: Automated Finite Element Computing. *ACM Trans. Math. Softw.*, 37(2): 20:1–20:28, April 2010. ISSN 0098-3500. doi: 10.1145/1731022.1731030. URL http://doi.acm.org/10.1145/1731022.1731030.

[60] A. Logg, K-A. Mardal, and G. Wells, editors. *Automated Solution of Differential Equations by the Finite Element Method*, volume 84 of *Lecture Notes in Computational Science and Engineering*. Springer-Verlag Berlin and Heidelberg, 1 edition, 2012. ISBN 978-3-642-23099-8. URL https://dx.doi.org/10.1007/978-3-642-23099-8.

[61] C. Lovadina. A New Class of Mixed Finite Element Methods for Reissner-Mindlin Plates. *SIAM Journal on Numerical Analysis*, 33(6):2457–2467, December 1996. ISSN 0036-1429. URL http://www.jstor.org/stable/2158480.

[62] A. E. H. Love. *A treatise on the mathematical theory of elasticity*. Cambridge University Press, 2013.

[63] N. Lu and D. Kim. Flexible and Stretchable Electronics Paving the Way for Soft Robotics. *Soft Robotics*, 1(1): 53–62, July 2013. ISSN 2169-5172. doi: 10.1089/soro.2013.0005. URL https://www.liebertpub.com/doi/abs/10.1089/soro.2013.0005.

[64] E. H. Mansfield. Bending, buckling and curling of a heated thin plate. *Proceedings of the Royal Society of London. Series A, Mathematical and Physical Sciences*, 268(1334):316–327, 1962. ISSN 00804630. URL http://www.jstor.org/stable/2414149.

[65] E.H. Mansfield. *The bending and stretching of plates*. Cambridge University Press, Cambridge, UK, 1989.

[66] C. Mardare. On the derivation of nonlinear shell models from three-dimensional elasticity. *Rev. Roumaine Maths. Pures Appl.*, 53:499–522, 2008.

[67] K. Marguerre. Zur theorie der gekrümmten platte grosser formänderung. In *Proceedings of the 5th international congress for applied mechanics*, pages 93–101, 1938.

[68] J. Marigo, C. Maurini, and K. Pham. An overview of the modelling of fracture by gradient damage models. *Meccanica*, 51(12):3107–3128, 2016.

[69] S. Micheletti and S. Perotto. Reliability and efficiency of an anisotropic Zienkiewicz-Zhu error estimator. *Computer Methods in Applied Mechanics and Engineering*, 195(9-12):799–835, 2006.

[70] R. D. Mindlin. Influence of rotatory inertia and shear on flexural motions of isotropic, elastic plates. *J. appl. Mech.*, 18:31, 1951.

[71] P. M. Naghdi. Foundations of elastic shell theory. Technical report, California Univ Berkeley Inst of Engineering Research, 1962.

[72] P. M. Naghdi. The theory of shells and plates. In *Linear Theories of Elasticity and Thermoelasticity*, pages 425–640. Springer, 1973.

[73] J. C. Nedelec. Mixed finite elements in R3. *Numerische Mathematik*, 35(3):315–341, September 1980. ISSN 0029-599X. doi: 10.1007/BF01396415. URL http://www.springerlink.com/content/vv750g6576n9p820/.

[74] T. D. Nguyen and G. N. Wells. Geometrically nonlinear formulation for thin shells without rotation degrees of freedom. *Computer Methods in Applied Mechanics and Engineering*, 197(33):2778 – 2788, 2008. ISSN 0045-7825. doi: https://doi.org/10.1016/j.cma.2008.01.001. URL http://www.sciencedirect.com/science/article/pii/S004578250800025X.

[75] V. P. Nguyen, C. Anitescu, S. P. A. Bordas, and T. Rabczuk. Isogeometric analysis: An overview and computer implementation aspects. *Mathematics and Computers in Simulation*, 117:89–116, November 2015. ISSN 0378-4754. doi: 10.1016/j.matcom.2015.05.008. URL http://www.sciencedirect.com/science/article/pii/S0378475415001214.

[76] N. Nguyen-Thanh, T. Rabczuk, H. Nguyen-Xuan, and S. P. A. Bordas. A smoothed finite element method for shell analysis. *Computer Methods in Applied Mechanics and Engineering*, 198(2):165–177, December 2008. ISSN 0045-7825. doi: 10.1016/j.cma.2008.05.029. URL http://www.sciencedirect.com/science/article/pii/S0045782508002090.

[77] J. Pommier and Y. Renard. *Getfem++, an open source generic C++ library for finite element methods*. 2005. URL http://getfem.org/.

[78] P. Råback, M. Malinen, J. Ruokolainen, A. Pursula, and T. Zwinger. Elmer models manual. *CSC–IT Center for*

Science, Helsinki, Finland, 2013.

[79] P. A. Raviart and J. M. Thomas. A mixed finite element method for 2-nd order elliptic problems. In Ilio Galligani and Enrico Magenes, editors, *Mathematical Aspects of Finite Element Methods*, pages 292–315, Berlin, Heidelberg, 1977. Springer Berlin Heidelberg. ISBN 978-3-540-37158-8.

[80] E. Reissner. On bending of elastic plates. *Quarterly of Applied Mathematics*, 5(1):55–68, 1947.

[81] J. A. Rogers, T. Someya, and Y. Huang. Materials and Mechanics for Stretchable Electronics. *Science*, 327(5973):1603–1607, March 2010. ISSN 0036-8075, 1095-9203. doi: 10.1126/science.1182383. URL http://science.sciencemag.org/content/327/5973/1603.

[82] M. E. Rognes, R. C. Kirby, and A. Logg. Efficient Assembly of $H(\mathrm{div})$ and $H(\mathrm{curl})$ Conforming Finite Elements. *SIAM Journal on Scientific Computing*, November 2009. doi: 10.1137/08073901X. URL http://epubs.siam.org/doi/abs/10.1137/08073901X.

[83] M. E. Rognes, D. A. Ham, C. J. Cotter, and A. T. T. McRae. Automating the solution of PDEs on the sphere and other manifolds in FEniCS 1.2. *Geoscientific Model Development*, 6(6):2099–2119, December 2013. ISSN 1991-9603. doi: 10.5194/gmd-6-2099-2013. URL http://www.geosci-model-dev.net/6/2099/2013/.

[84] B. Roman. Fracture path in brittle thin sheets: a unifying review on tearing. *International Journal of Fracture*, 182(2):209–237, 2013. ISSN 1573-2673. doi: 10.1007/s10704-013-9869-5. URL http://dx.doi.org/10.1007/s10704-013-9869-5.

[85] Karam S. and Arthur L. *Homogenization of Heterogeneous Thin and Thick Plates*. Wiley-Blackwell, 2015. ISBN 9781119005247. doi: 10.1002/9781119005247. URL https://onlinelibrary.wiley.com/doi/abs/10.1002/9781119005247.

[86] J. Sanchez-Hubert and E. Sanchez-Palencia. *Coques élastiques minces: propriétés asymptotiques*. Masson edition, 1997.

[87] E. Sanchez-Palencia, O. Millet, and F. Béchet. *Singular Problems in Shell Theory: Computing and Asymptotics*. Number 54 in Lecture Notes in Applied and Computational Mechanics. Springer-Verlag, 2010.

[88] K. A. Seffen and S. D. Guest. Prestressed morphing bistable and neutrally stable shells. *Journal of Applied Mechanics, Transactions ASME*, 78(1):011002–1 to 011002–6, 2011.

[89] K.A. Seffen. Morphing bistable orthotropic elliptical shallow shells. *Proceedings of the Royal Society A: Mathematical, Physical and Engineering Sciences*, 463:67–83, 2007.

[90] K.A. Seffen and C. Maurini. Growth and shape control of disks by bending and extension. *Journal of the Mechanics and Physics of Solids*, 61(1):190–204, 2013. doi: 10.1016/j.jmps.2012.08.003. URL http://www.scopus.com/inward/record.url?eid=2-s2.0-84867574320&partnerID=40&md5=0db3ce9b07bc5a4090db32d135a60165.

[91] J. C Simo and M. S Rifai. A class of mixed assumed strain methods and the method of incompatible modes. *International Journal for Numerical Methods in Engineering*, 29(8):1595–1638, June 1990. ISSN 1097-0207. doi: 10.1002/nme.1620290802. URL http://onlinelibrary.wiley.com/doi/10.1002/nme.1620290802/abstract.

[92] K. Y. Sze, X. H. Liu, and S. H. Lo. Popular benchmark problems for geometric nonlinear analysis of shells. *Finite elements in analysis and design*, 40(11):1551–1569, 2004.

[93] P. Vannucci, B. Cochelin, N. Damil, and M. Potier-Ferry. An asymptotic-numerical method to compute bifurcating branches. *International Journal for Numerical Methods in Engineering*, 41(8):1365–1389, December 1998. doi: 10.1002/(SICI)1097-0207(19980430)41:8⟨1365::AID-NME332⟩3.0.CO;2-Y. URL https://onlinelibrary.wiley.com/doi/abs/10.1002/%28SICI%291097-0207%2819980430%2941%3A8%3C1365%3A%3AAID-NME332%3E3.0.CO%3B2-Y.

[94] T. Von Kármán. *Festigkeitsprobleme im maschinenbau*. Teubner, 1910.

[95] G. N. Wells and T. D. Nguyen. A c0 discontinuous galerkin formulation for kirchhoff plates. *Computer Methods in Applied Mechanics and Engineering*, 196(35):3370 – 3380, 2007. ISSN 0045-7825. doi: https://doi.org/10.1016/j.cma.2007.03.008. URL http://www.sciencedirect.com/science/article/pii/S0045782507001429.

[96] G. Wilson, D. A. Aruliah, C. T. Brown, Neil P. Chue Hong, Matt Davis, Richard T. Guy, Steven H. D. Haddock, Kathryn D. Huff, Ian M. Mitchell, Mark D. Plumbley, Ben Waugh, Ethan P. White, and Paul Wilson. Best Practices for Scientific Computing. *PLOS Biology*, 12(1):e1001745, January 2014. ISSN 1545-7885. doi: 10.1371/journal.pbio.1001745. URL http://journals.plos.org/plosbiology/article?id=10.1371/journal.pbio.1001745.